University of California

Los Angeles

Numerical Studies of Turbulence in LAPD

A dissertation submitted in partial satisfaction

of the requirements for the degree

Doctor of Philosophy in Physics

by

Brett Cory Friedman

2013

Abstract of the Dissertation

Numerical Studies of Turbulence in LAPD

by

Brett Cory Friedman

Doctor of Philosophy in Physics

University of California, Los Angeles, 2013

Professor Troy A. Carter, Chair

To be completed

The dissertation of Brett Cory Friedman is approved.

Warren B. Mori

George J. Morales

Russel E. Caflisch

Troy A. Carter, Committee Chair

University of California, Los Angeles

2013

To be completed . . .

TABLE OF CONTENTS

List of Figures

List of Tables

Acknowledgments

To be completed . . .

Vita

2003-2007	Regent Scholar, University of California, Irvine.
2007	B.S. (Physics) Summa Cum Laude, University of California, Irvine.
2007	Chancellor's Fellow, University of California, Los Angeles.
2007-2009	Teaching Assistant, Department of Physics and Astronomy, University of California, Los Angeles.
2009-2013	Research Assistant, Department of Physics and Astronomy, University of California, Los Angeles.
2009-2012	ORISE FES Fellow, University of California, Los Angeles.
2012-2013	Dissertation Year Fellow, University of California, Los Angeles.

PUBLICATIONS

B. Friedman, T. A. Carter, M. V. Umansky, D. Schaffner, and B. Dudson, Energy dynamics in a simulation of LAPD turbulence, Phys. Plasmas 19, 102307 (2012).

D. A. Schaffner, T. A Carter, G. D. Rossi, D. S. Guice, J. E. Maggs, S. Vincena, and B. Friedman, Modification of Turbulent Transport with Continuous Variation of Flow Shear in the Large Plasma Device, Phys. Rev. Lett. 109, 135002 (2012).

S. Zhou, W. W. Heidbrink, H. Boehmer, R. McWilliams, T. A. Carter, S. Vincena, B. Friedman, and D. Schaffner, Sheared-flow induced confinement transition in a linear magnetized plasma, Phys. Plasmas 19, 012116 (2012).

B. Friedman, M. V. Umansky, and T. A. Carter, Grid convergence study in a simulation of LAPD turbulence, Contrib. Plasma Phys. 52, 412 (2012).

M. V. Umansky, P. Popovich, T. A. Carter, B. Friedman, and W. M. Nevins, Numerical simulation and analysis of plasma turbulence the Large Plasma Device, Phys. Plasmas 18, 055709 (2011).

P. Popovich, M.V. Umansky, T.A. Carter, and B. Friedman, Modeling plasma turbulence and transport in the Large Plasma Device, Phys. Plasmas 17, 122312 (2010).

P. Popovich, M.V. Umansky, T.A. Carter, and B. Friedman, Analysis of plasma instabilities and verification of the BOUT code for the Large Plasma Device, Phys. Plasmas 17, 102107 (2010).

S. Zhou, W. W. Heidbrink, H. Boehmer, R. McWilliams, T. A. Carter, S. Vincena, S. K. P. Tripathi, P. Popovich, B. Friedman, and F. Jenko, Turbulent transport of fast ions in the Large Plasma Device, Phys. Plasmas 17, 092103 (2010).

CHAPTER 1

Introduction

CHAPTER 2

Turbulence and Instability

CHAPTER 3

The Braginskii Fluid Model and LAPD

3.1 LAPD Suitability to the Braginskii Fluid Model

At a basic level, the state of a plasma is described by seven-dimensional distribution functions $f_j(\mathbf{x}, \mathbf{v}, t)$ for each species j. The behavior of the plasma is described by the system of kinetic equations (Boltzmann equations), which evolve the distribution functions forward in time:

$$\frac{\partial f_j}{\partial t} + \mathbf{v} \cdot \nabla f_j + \frac{e_j}{m_j}(\mathbf{E} + \mathbf{v} \times \mathbf{B}) \cdot \frac{\partial f_j}{\partial \mathbf{v}} = \left(\frac{\partial f_j}{\partial t}\right)_C. \tag{3.1}$$

$\left(\frac{\partial f_j}{\partial t}\right)_C$ is the change in the distribution function due to collisions. For plasmas, the collisions are Coulomb collisions, and the collision term takes the form of the Fokker-Planck operator. With this operator, Eq. 3.1 is called the Fokker-Planck equation. Now it is well known that the Fokker-Planck equation cannot be solved numerically for problems that require time intervals much larger than the electron-cyclotron time due to computational and time limitations. The phase space is just too large. Therefore, reduced equations, such as gyrokinetic, drift kinetic, or fluid equations have been derived to produce numerically tractable equations. These equations are all derived under certain physical assumptions such as strong guiding magnetic fields, small fluctuation levels, or slow spatial and/or time variations such that these different equations are best applied to different physical situations.

The equations that are arguably most suitable to describe waves and turbulence in LAPD (and fastest to solve numerically) are the fluid equations, specif-

ically those derived by Braginskii [Bra65]. In deriving his equations, Braginskii approximates the solution as $f_j = f_j^0 + f_j^1$ where the zero-order piece f_j^0 is a Maxwellian and the first-order piece f_j^1 is a perturbation on the zero-order distribution function: $|f_j^1| \ll f_j^0$. The equations are then derived by taking moments of the Fokker-Planck equation to create coupled equations of the independent variables, n_j, $\mathbf{v_j}$, and T_j. Now certain requirements must hold to justify the Braginskii approximation, all of which have the flavor that macroscopic quantities must vary slowly in time and space. This is generally caused by strong relaxation processes such as collisions, which keep the distribution functions close to Maxwellians. In general, for the Braginskii equations to be applicable, processes of interest must occur on time intervals much greater than the collision time and quantities should vary slowly over distances traversed by the particles between collisions.

Specifically, the requirement that time variations must be slow can be written $\frac{d}{dt} \ll \nu$, where for electron drift wave turbulence, this is approximately $\omega_* \ll \nu_e$. Table 4.3, which displays typical LAPD operating parameters, shows that $\omega_*/\nu_e \sim 0.01$. The requirement that spatial quantities vary slowly compared to the collisional mean free path can be written simply for the direction parallel to the magnetic field as $\lambda_{ei} \sim \lambda_{ee} \ll L_\parallel$. For LAPD, $\lambda_{ei}/L_\parallel \sim 0.01$. For the direction perpendicular to the magnetic field, the same kind of relation $\lambda_{mfp} \ll L_\perp$ must also hold. However, due to the cyclotron motion of particles around the magnetic field, λ_{mfp} is really the larmor radius, unless the collisional mean free path is less than the larmor radius. For electrons, $\rho_e \ll \lambda_{ei}$ and $\rho_e/L_\perp \sim 10^{-4}$ where $L_\perp \sim 0.1$ m. For the ions, the ion cyclotron frequency is close to the ion collision frequency, meaning that either the ion larmor radius or the ion mean free path may be used. Using the larmor radius, $\rho_i/L_\perp \sim 0.01$. Therefore, the collisionality is high enough and the machine dimensions are large enough so that the Braginskii fluid model should be applicable to LAPD.

3.2 The Braginskii Equations

The Braginskii fluid equations are as follows: the continuity equation for species j, electrons or ions, is [Wes04, Bra65]

$$\frac{\partial n_j}{\partial t} = -\nabla \cdot (n_j \mathbf{v}_j).$$

(3.2)

The momentum balance equation is

$$n_j m_j \frac{d\mathbf{v}_j}{dt} = -\nabla p_j - \frac{\partial \Pi_{j\alpha\beta}}{\partial x_\beta} + n_j e_j (\mathbf{E} + \mathbf{v_j} \times \mathbf{B}) + \mathbf{R}_j.$$

(3.3)

$p_j = n_j T_j$ is the pressure. $\Pi_{j\alpha\beta}$ is the stress tensor, which involves the products of viscosity coefficients and rate-of-strain tensor components. The viscosity coefficients are some of the several terms that are called transport coefficients. The transport coefficients are calculated by the Braginskii procedure in terms of n, $\mathbf{v}$, and T. $\mathbf{R}_j$, which involves several other transport coefficients, is the rate of collional momentum transfer. The momentum transfer from ions to electrons is given by

$$\mathbf{R}_e = -m_e n_e \nu_e (0.51 u_{\|e} + \mathbf{u}_{\perp e}) - 0.71 n_e \nabla_\| T_e - \frac{3}{2} \frac{n_e \nu_e}{\omega_{ce}} \mathbf{b} \times \nabla T_e$$

(3.4)

where $\mathbf{u} = \mathbf{v}_e - \mathbf{v}_i$ and ν_e is the electron collision frequency with ions. $\mathbf{R}_e$ includes both the friction force and the thermal force, which, like the friction force, is due to electron-ion collisions, but originates from the temperature dependence of the collisionality. The thermal force terms are those proportional to the gradients of temperature. $\mathbf{R}_i = -\mathbf{R}_e$ in a fully ionized plasma with one ion species. However, LAPD has a significant neutral density. Collisions with neutrals are much more important for the ions [PUC10a]. So

$$\mathbf{R}_i = -\mathbf{R}_e - n_i m_i \nu_{in} \mathbf{v_i}.$$

(3.5)

The energy balance equation is

$$\frac{3}{2}n_j\frac{\partial T_j}{\partial t} = -n\mathbf{v}_j \cdot \nabla T_j - p_j\nabla \cdot \mathbf{v}_j - \nabla \cdot \mathbf{q}_j - \Pi_{j\alpha\beta}\frac{\partial v_j\alpha}{\partial x_\beta} + Q_j \qquad (3.6)$$

where the term involving the stress tensor describes viscous heating. The electron heat flux (with more transport coefficients) is

$$q_e = n_eT_e\left(0.71u_\parallel + \frac{3\nu_e}{2\omega_{ce}}\mathbf{b}\times\mathbf{u}\right)$$
$$+\frac{n_eT_e}{m_e\nu_e}\left(-3.16\nabla_\parallel T_e - \frac{4.66\nu_e^2}{\omega_{ce}^2}\nabla_\perp T_e - \frac{5\nu_e}{2\omega_{ce}}\mathbf{b}\times\nabla T_e\right) \qquad (3.7)$$

where the first part of this expression constitutes convection, while the second part is conduction. The ion heat flux is

$$q_i = \frac{n_iT_i}{m_i\nu_i}\left(-3.9\nabla_\parallel T_i - \frac{2\nu_i^2}{\omega_{ci}^2}\nabla_\perp T_i - \frac{5\nu_i}{2\omega_{ci}}\mathbf{b}\times\nabla T_i\right). \qquad (3.8)$$

The last transport coefficients are in the heating Q. The ion heating due to collisional heat exchange between ions and electrons is

$$Q_i = \frac{3m_e}{m_i}n_e\nu_e(T_e - T_i) \qquad (3.9)$$

while the electron heating is

$$Q_e = -\mathbf{R}\cdot\mathbf{u} - Q_i. \qquad (3.10)$$

The electron heat exchange involves an ohmic heating contribution $(\mathbf{R}\cdot\mathbf{u})$ that is absent from the ion heating because electrons colliding with ions transfer very little momentum to the ions.

6

3.3 The Vorticity Equation

Now the Braginskii equations in the previous section contain electric and magnetic fields which must be self-consistently determined by the charges and currents that are evolved by the equations. This is done with the inclusion of Maxwell's equations. Two of those equations are used to write the fields in terms of potentials:

$$\mathbf{E} = -\nabla\phi - \frac{\partial \mathbf{A}}{\partial t} \tag{3.11}$$
$$\mathbf{B} = \nabla \times \mathbf{A}.$$

The vector potential $\mathbf{A}$ is strictly a fluctuating quantity, meaning it is not used to describe the guide field $\mathbf{B}_0$. The next equation,

$$\nabla \times \mathbf{B} = \nabla(\nabla \cdot \mathbf{A}) - \nabla^2 \mathbf{A} = \mu_0 \mathbf{j} \tag{3.12}$$

is used to relate the vector potential to the current, where the displacement current is neglected as is generally done in plasmas. The Poisson equation is not that useful for the main part of the plasma, in which the quasineutrality relation, $n_e = n_i \equiv n$, holds. The useful equation that can be used instead is the conservation of charge (or ambipolarity condition), $\nabla \cdot \mathbf{j} = 0$. The vorticity equation is derived from this conservation of charge equation.

The current is $\mathbf{j} = en(v_{\parallel i} - v_{\parallel e}) + en(\mathbf{v}_{\perp i} - \mathbf{v}_{\perp e})$. In LAPD, the parallel current is carried primarily by the fast streaming electrons, while the perpendicular current is primarily carried by the ions, which have larger Larmor radii. So the conservation of charge equation can be simplified to

$$\nabla_\parallel (nv_{\parallel e}) = \nabla_\perp \cdot (n\mathbf{v}_{\perp i}). \tag{3.13}$$

The perpendicular ion component of this equation is derived from Eq. 3.3

for the ions. Neglecting terms that have finite ion temperature (pressure and stress tensor), and solving for the ion velocity in the Lorentz force term, the perpendicular ion velocity has three terms [PUC10a, SC03]:

$$\mathbf{v}_{\perp i} = \mathbf{v}_E + \mathbf{v}_{pi} + \mathbf{v}_{\nu i} \tag{3.14}$$

where the $\mathbf{E} \times \mathbf{B}$ velocity is $\mathbf{v}_E = \mathbf{E} \times \mathbf{B}/B^2 = -\nabla_\perp \phi \times \mathbf{B}/B^2$, the polarization velocity is $\mathbf{v}_{pi} = (1/\omega_{ci})\mathbf{b} \times (\partial_t + \mathbf{v}_i \cdot \nabla)\mathbf{v}_i$, and the Pedersen velocity is $\mathbf{v}_{\nu i} = (\nu_{in}/\omega_{ci})\mathbf{b} \times \mathbf{v}_i$. The charge conservation equation then takes the form:

$$\nabla_\parallel(nv_{\parallel e}) = \frac{1}{\omega_{ci}}\nabla_\perp \cdot [n\mathbf{b} \times (\partial_t + \mathbf{v}_i \cdot \nabla + \nu_{in})\mathbf{v}_i]. \tag{3.15}$$

Note that the $\mathbf{E} \times \mathbf{B}$ velocity doesn't contribute to the current due to the electrons producing an equal and opposite $\mathbf{E} \times \mathbf{B}$ current. I now employ the approximation $\mathbf{v}_i \sim \mathbf{v}_E$ to Eq. 3.15. This approximation wasn't appropriate of course for Eq. 3.14 due to the fact that $\mathbf{v}_E$ doesn't contribute to the current, but it is appropriate here. Then,

$$\nabla_\parallel(nv_{\parallel e}) = \frac{1}{\omega_{ci}}\nabla_\perp \cdot [n\mathbf{b} \times (\partial_t + \mathbf{v}_E \cdot \nabla + \nu_{in})\mathbf{v}_E] \rightarrow \tag{3.16}$$
$$\nabla_\parallel(nv_{\parallel e}) = -\frac{m_i}{eB^2}\nabla_\perp \cdot [n\mathbf{b} \times (\partial_t + \mathbf{v}_E \cdot \nabla + \nu_{in})\nabla_\perp \phi].$$

Next, defining the vorticity as $\varpi \equiv \nabla_\perp \cdot (n\nabla_\perp \phi)$, the vorticity equation reads,

$$\frac{\partial \varpi}{\partial t} = -\mathbf{v}_E \cdot \nabla_\perp \varpi - \nabla_\perp \mathbf{v}_E : \nabla_\perp(n\nabla_\perp \phi) - \frac{eB^2}{m_i}\nabla_\parallel(nv_{\parallel e}) - \nu_{in}\varpi. \tag{3.17}$$

Finally, the term with the tensor product can be rewritten in a different form [PUC10a]:

$$\frac{\partial \varpi}{\partial t} = -\mathbf{v}_E \cdot \nabla_\perp \varpi + \frac{1}{2}(\mathbf{b} \times \nabla_\perp n) \cdot \nabla_\perp \mathbf{v}_E^2 - \frac{eB^2}{m_i}\nabla_\parallel(nv_{\parallel e}) - \nu_{in}\varpi. \tag{3.18}$$

3.4 Minimizing the Equation Set for LAPD Parameters

3.4.1 The Reduced Equations

The continuity equations 3.2 for electrons and ions do not have to both be used due to the quasineutrality condition $n_e = n_i \equiv n$. So, if one focuses on the electron continuity equation, then,

$$\frac{\partial n}{\partial t} = -\nabla \cdot (n\mathbf{v}_e). \tag{3.19}$$

Now, $\mathbf{v}_e = \mathbf{v}_{\perp e} + v_{\parallel e}$, where $\mathbf{v}_{\perp e} = \mathbf{v}_E + \mathbf{v}_{de} + \mathbf{v}_{pe}$, with the diamagnetic velocity $\mathbf{v}_{de} = \frac{\mathbf{b} \times \nabla p_e}{e n_e B}$, which wasn't included for the ions in Eq. 3.14 due to the neglect of ion pressure. To a good approximation, the electron polarization velocity is smaller than the $\mathbf{E} \times \mathbf{B}$ velocity, so that $\nabla \cdot (n\mathbf{v}_{\perp e}) = \mathbf{v}_E \cdot \nabla n$ [PUC10a, SC03]. So, the continuity equation reads

$$\frac{\partial n}{\partial t} = -\mathbf{v}_E \cdot \nabla n - \nabla_{\parallel}(n v_{\parallel e}). \tag{3.20}$$

Next, the momentum equations (Eq. 3.3), of which there are six (three for electron velocity components and three for ion velocity components) are reduced to two here. The first is the vorticity equation (Eq. 3.18), in which I used the perpendicular momentum equations to derive it. The second is the equation for the parallel electron momentum. I neglect the parallel ion momentum equation since $v_{\parallel e} \gg v_{\parallel i}$ for LAPD. The electron parallel momentum equation is then

$$nm_e \frac{\partial v_{\parallel e}}{\partial t} = -nm_e \mathbf{v}_E \cdot \nabla v_{\parallel e} - \nabla_{\parallel} p_e - enE_{\parallel} - 0.71 n \nabla_{\parallel} T_e - 0.51 m_e n \nu_e v_{\parallel e}, \tag{3.21}$$

where the viscous terms have been neglected. The conservation of energy equations (Eq. 3.6) are left. Since the ion temperature in LAPD is very low

$(T_i \leq 1$ eV), the ion energy equation is neglected. The electron energy equation is [SC03]

$$\frac{3}{2}n\frac{\partial T_e}{\partial t} = -\frac{3}{2}n\mathbf{v}_E \cdot \nabla T_e - p_e\nabla_\| v_{\|e} + 0.71T_e\nabla \cdot (nv_{\|e})$$
$$+\nabla_\|(\kappa_{\|e}\nabla_\| T_e) + 0.51m_e n\nu_e v_{\|e}^2 - 3\frac{m_e}{m_i}n\nu_e T_e, \tag{3.22}$$

where $\kappa_{\|e} = 3.16\frac{nT_e}{m_e\nu_e}$.

3.4.2 The Electrostatic Justification

Plasma currents create magnetic fields in plasmas. Often times, analytic and numerical calculations of plasma waves and turbulence neglect the time dependent magnetic field perturbations, focusing only on the electrostatic contribution to the waves, turbulence, and transport. In the reduced fluid equations of the previous subsection, the magnetic perturbation enters in two important ways. First, it enters the electric field term of Eq. 3.21 because $E_\| = -\nabla_\|\phi - \frac{\partial A_\|}{\partial t}$, where $A_\|$ is the parallel component of the vector potential. Second, it affects the parallel gradient operator, $\nabla_\| = \mathbf{b} \cdot \nabla$ where $\mathbf{b}$ is in the direction of the total magnetic field [SC03]. In the electrostatic limit, $A_\| \to 0$, so $E_\| = -\nabla_\|\phi$ and $\nabla_\| = \mathbf{b_0} \cdot \nabla$. I take this limit in the remaining chapters, but there is the question of how justified I am to do so.

As a first step in answering this question, examine Eq. 3.21. The four independent variables, $n, \phi, v_{\|e}$, and T_e, which each have their own evolution equation, are all present in Eq. 3.21. Taking the parallel projection of Eq. 3.12 gives

$$\nabla_\perp^2 A_\| = -\mu_0 j_\| = \mu_0 n e v_{\|e}. \tag{3.23}$$

So $A_\| \sim \mu_0 n e L_\perp^2 v_{\|e}$, where $\nabla_\perp^2 \sim 1/L_\perp^2$. Then, Eq. 3.21 can be approximately rewritten as,

$$nm_e\frac{dv_{\parallel e}}{dt} \sim -T_e\nabla_\parallel n+en\nabla_\parallel\phi+\mu_0 e^2 n^2 L_\perp^2\frac{\partial v_{\parallel e}}{\partial t}-1.71n\nabla_\parallel T_e-0.51m_e n\nu_e v_{\parallel e}. \quad (3.24)$$

The electromagnetic induction term, ($EM = en\frac{\partial A_\parallel}{\partial t}$) is now written in terms of $v_{\parallel e}$ as $EM = \mu_0 e^2 n^2 L_\perp^2\frac{\partial v_{\parallel e}}{\partial t}$. It can therefore be directly compared to the other terms proportional to $v_{\parallel e}$ to test for its importance. The other terms are the inertial term, $M = nm_e\frac{dv_{\parallel e}}{dt}$ and the resistive term, $R = 0.51m_e n\nu_e v_{\parallel e}$. A common way to compare these terms is to approximate the time derivative as the ion cyclotron frequency $\frac{\partial}{\partial t} \sim \omega_{ci}$ and the perpendicular length scale as the ion sound gyroradius $L_\perp \sim \rho_s$, where $\rho_s = c_s/\omega_{ci}$. Then the ratio of the three terms (obtained by dividing each term by $eBnv_{\parallel e}$) is:

$$M : EM : R = \frac{m_e}{m_i} : \beta : \frac{0.51\nu_e}{\omega_{ce}}. \quad (3.25)$$

It can be seen from Table 4.3 that in LAPD, this ratio is 1 : 3.6 : 1.5. Thus, all three terms are of the same order with the electromagnetic term slightly larger than the other two. It seems then quite unjustified to use an electrostatic approximation.

However, estimating $\frac{\partial}{\partial t} \sim \omega_{ci}$ isn't necessarily accurate. The equation set describes drift waves and so a more proper estimate might be $\frac{\partial}{\partial t} \sim \omega_*$. Under this approximations, the ratio is 1 : 3.6 : 70, meaning that the resistive term is more than an order of magnitude larger than the other two; however, the approximation $\frac{\partial}{\partial t} \sim \omega_*$ is still rough and the numerical value of ω_* in Table 4.3 is somewhat of a rough itself. Moreover, one could also argue with the approximation of the perpendicular length scale as the sound gyroradius. This is probably too small, in which case the electromagnetic inductance has been underestimated. While it's clear that the inertial term is probably unimportant, the inductive term could be important.

Similarly, the contribution of $\tilde{\mathbf{b}} \sim A_\parallel$ in $\nabla_\parallel$ can be approximated in a similar manner with similar inconclusive results. Without a clear separation between the resistive and inductive terms, the best way to determine the validity of the electrostatic approximation is by direct numerical calculation of the turbulence with and without the electromagnetic contributions. Therefore, I simulated an electrostatic and two electromagnetic versions of LAPD turbulence. The details of the electrostatic code are described in Chapter 4 and in Appendix A.

The only difference between the electrostatic and the first electromagnetic simulation is the exclusion/inclusion of the electromagnetic term $en\frac{\partial A_\parallel}{\partial t}$ in the parallel electron momentum equation (Eq. 3.21). Of course the Maxwell equation (Eq. 3.12) must also be included for the electromagnetic simulation. The second electromagnetic simulation includes not only this term but also the $A_\parallel$ contribution to $\nabla_\parallel$ in the parallel electron momentum equation.

Now, turbulence is best characterized and compared in a statistical and often spectral manner. More details of turbulence characterization and comparison will be discussed later, but for now, I make a few statistical comparisons between the electrostatic and electromagnetic simulation results. Figure 3.1 shows the results of the three simulations as well as the experiment – namely, a comparison of the frequency spectra, the probability distribution function (pdf), and the rms level of the density fluctuations. The "Full Electromagnetic" curves are from the simulation including the $A_\parallel$ contribution to $\nabla_\parallel$, while the "Electromagnetic" curves just include the $A_\parallel$ contribution to $E_\parallel$. Clearly, the fluctuations are statistically similar in all cases and none of the simulations are inconsistent with the experiment. However, the electromagnetic effects are noticable, and as I include more electromagnetic contributions in the simulations, the turbulent statistics more closely resemble those of the experiment. I make no quantitative comparison here, but rely only on a visual examination in making this conclusion.

Now, as mentioned above, I do not include any electromagnetic contributions

in the simulations used in the following chapters. It seems rather unjustified to do so since I am clearly able to run electromagnetic simulations and they seem to reproduce experimental turbulence with slightly better accuracy than the electrostatic ones. One justification for my abandonment of electromagnetic simulations, however, is that electromagnetic simulations take a bit longer than electrostatic ones due to the extra relation in Eq. 3.12 that is used to solve for $A_\parallel$, which requires an inversion of the Laplacian. This takes extra computation. Another justification is that the electromagnetic equations make the energy dynamics analysis in Chapter 6 a bit more complicated. Both of these factors are mitigated, however, if the inertial term $nm_e \frac{dv_{\parallel e}}{dt}$ is dropped. Nevertheless, at the beginning of this work, I strived to find the simplest possible model to describe the turbulence in LAPD, and I determined that the electrostatic approximation was acceptable. At that time, I didn't have the results of Fig. 3.1. If I had the time, I would redo all of the simulations and analysis to include electromagnetic contributions, but drop the inertial term in Eq. 3.21. This is a clear route to take for future work. Nevertheless, I am confident that electromagnetics would not change any of my conclusions in this work. So for the remainder of this work, I will present theoretical calculations, simulation results, and conclusions using the electrostatic approximation.
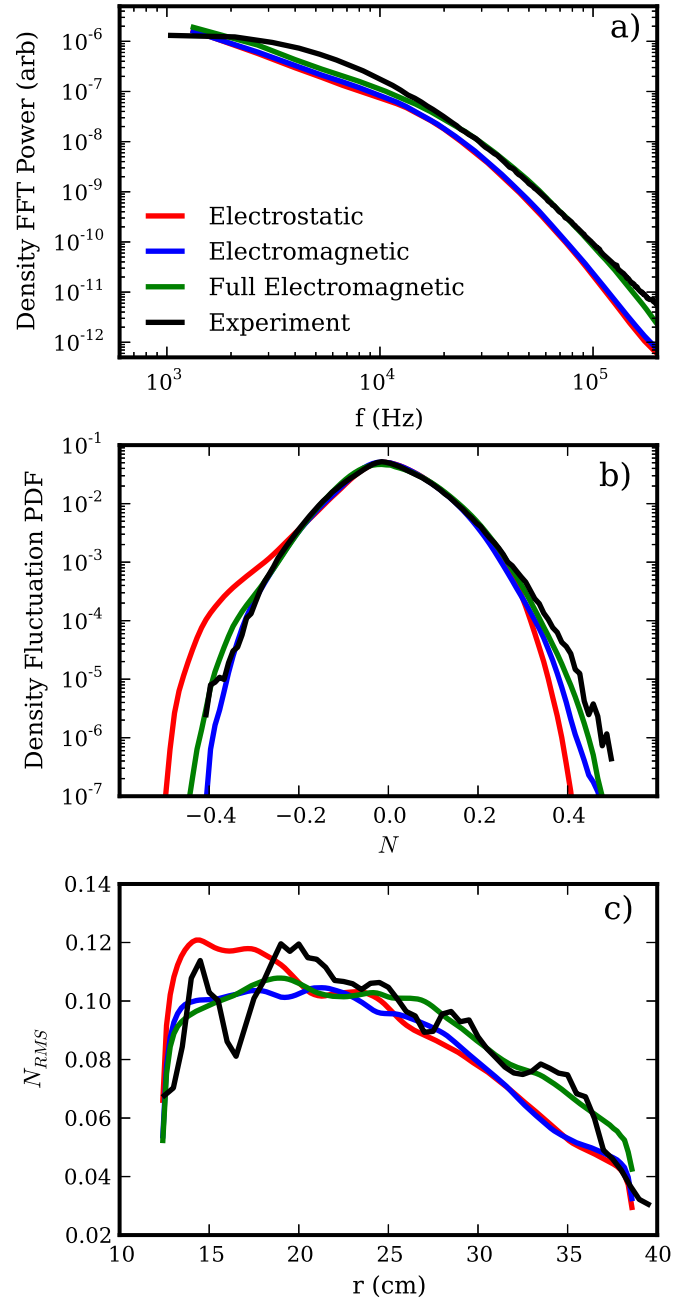
Figure 3.1: Electromagnetic statistics comparison

CHAPTER 4

LAPD Simulation Details

In this chapter, I state and explain the equations, boundary conditions, parameters, and profiles that I use in the LAPD simulations. There are two main classes of simulations: those with a mean radial electric field and those without. The simulations with the mean radial electric field will be explored in Chapter 9. This chapter and all those up to Chapter 9 deal with the simulations with no mean radial electric field. There are only four different simulations that are used until Chapter 9, and they differ in only one way: their axial boundary conditions, which are explained in Sec. 4.2.

I solve the equations using the BOUT++ code [DUX09]. The code is discussed and partially displayed in Appendix A, and specific numerical routines and other details are described there as well.

4.1 The Equations

I use the Braginskii equations as shown in Chapter 3 to model LAPD turbulence. I separate all variables into time-independent equilibrium parts and time-dependent fluctuating parts. I do this in order to input experimental time-independent profiles. The alternative would be to solve the full equations with no equilibrium/fluctuation separation and no experimental profile input. The difficulty in this alternative technique is the need to specify sources, sinks, and boundary conditions, which can be difficult to measure or estimate. This alternative method has

15

been untertaken by Rogers and Ricci [RR10]. Our approach is easier, and since the time-independent profiles are so important in driving the turbulence, I feel that inputing the experimentally measured profiles can help produce physically realistic turbulence.

Now due to the equilibrium/fluctuation separation technique, I can linearize the equations, keeping only one nonlinearity in each equation: the advective non-linearity. While this isn't necessary, it does simplify the energy dynamics as formulated in Chapter 6. The justification is practical rather than mathematical, and the partially linearized equations produce fluctuations that are quite statistically similar to experimental fluctuations, which is shown in Chapter 5, so I feel justified in doing this.

In the equations below, I normalize all quantities to give dimensionless variables. All times are normalized to the inverse ion cyclotron frequency $\omega_{ci} = \frac{eB}{m_i}$, velocities are normalized to the ion sound speed $c_s = \sqrt{\frac{T_e}{m_i}}$, lengths are normalized to the sound gyro-radius $\rho_s = c_s/\omega_{ci}$, potentials to T_e/e, densities to the density at the radial cylindrical axis, and temperatures to the temperature at the cylindrical axis. Quantities such as c_s that are typically functions of radius due to the radial dependence of the electron temperature are taken to be constant in these normalizations, where I use the values at the radial axis. The equations below don't reflect this, but the transport coefficients in the actual code do. So, the LAPD simulation equations are as follows:

$$\partial_t N = -\mathbf{v_E} \cdot \nabla N_0 - N_0 \nabla_\parallel v_{\parallel e} + \mu_N \nabla_\perp^2 N + S_N + \{\phi, N\}, \qquad (4.1)$$

$$\partial_t v_{\parallel e} = -\frac{m_i}{m_e}\frac{T_{e0}}{N_0}\nabla_\parallel N - 1.71\frac{m_i}{m_e}\nabla_\parallel T_e + \frac{m_i}{m_e}\nabla_\parallel \phi - \nu_e v_{\parallel e} + \{\phi, v_{\parallel e}\}, \qquad (4.2)$$

$$\partial_t \varpi = -N_0 \nabla_\parallel v_{\parallel e} - \nu_{in}\varpi + \mu_\phi \nabla_\perp^2 \varpi + \{\phi, \varpi\}, \qquad (4.3)$$

$$\partial_t T_e = -\mathbf{v_E} \cdot \nabla T_{e0} - 1.71\frac{2}{3}T_{e0}\nabla_\parallel v_{\parallel e} + \frac{2}{3N_0}\kappa_{\parallel e}\nabla_\parallel^2 T_e$$
$$-\frac{2m_e}{m_i}\nu_e T_e + \mu_T \nabla_\perp^2 T_e + S_T + \{\phi, T_e\}. \qquad (4.4)$$

Note that the advective nonlinearities in each equation are written with Poisson brackets. Additionally, the only equilibrium profiles are N_0 and T_{e0}, which are only functions of radius. $\phi_0 = v_{\parallel e0} = 0$ in these equations. The linearized vorticity is $\varpi = \nabla_\perp \cdot (N_0 \nabla_\perp \phi)$. $N, v_{\parallel e}, \phi$, and T_e are fluctuating first-order quantities.

These equations have a few additional terms not included in the equations of Chapter 3. First, I have included density and temperature sources S_N and S_T. I have left out a momentum source as well as the contribution of the density source to changes of the momentum and temperature. Second, I have included diffusive ($\mu_N \nabla_\perp^2 N$ and $\mu_T \nabla_\perp^2 T_e$) and viscous ($\mu_\phi \nabla_\perp^2 \varpi$) terms in Eqs. 4.1, 4.4, and 4.3 respectively.

4.1.1 Sources

The density source is actually a source/sink. It models both the ionization of neutral atoms as well as the recombination of ions and electrons. The sink action in LAPD is dominated by parallel (along **B**) losses to materials at the machine ends because the magnetic field prevents rapid radial loss. It's also possible that a layer of neutral atoms near the end of the machine opposite the cathode cools the plasma enough so that recombination can be strong in this layer. The sink action occurs at all radii with finite plasma density, which constitutes regions both inside and outside of the cathode radius due to radial ion transport. If the sink action is primarily at the end plates, the sink can be calculated by $2n_{se}c_s/L_\parallel$, where n_{se} is the density at the sheath edge in front of the end plate, c_s is the sound speed at the sheath edge, and the factor of 2 accounts for the two plates. n_{se} and c_s are functions of radius such that the sink is strongest at the radial axis and decreases at larger radii. Calculation of the sink term requires knowledge of the density and temperature at the end of the machine, which is generally not measured experimentally.

The ionization source occurs primarily inside of the cathode radius. The source term is calculated with $n_e n_n \langle \sigma v \rangle_{iz}$, where n_n is the neutral Helium density and $\langle \sigma v \rangle_{iz}$ is the ionization rate of Helium and is a strong function of temperature. The strong temperature dependence is the reason why ionization occurs only within the cathode radius. Ionization rates are readily available [Sta00], but the neutral density is not, making the source difficult to calculate. However, it is clear that if one were to sum up the source and sink and integrate axially, the region inside of the cathode radius must be a net source, while the region outside of it must be a net sink.

Now when I simulate the turbulence in LAPD without the source terms, turbulence drives radial transport such that the total flux-surface-averaged density gradient relaxes over time as seen in Fig. 4.1 a) until the radial transport ceases. It's interesting that $\langle N_t \rangle_{fs} = \langle N_0 + N \rangle_{fs}$ doesn't become totally flat, but maintains a gradient. This is probably a result of the partial linearization of the equations, especially the diffusion term $\mu_N \nabla_\perp^2 N$, and possibly boundary conditions. Nevertheless, the strong relaxation is not physical due to the presence of the physical source/sink mechanism. (Note that the equilibrium density profile N_0 used in the simulation to make Fig. 4.1 a) is not the same N_0 shown in Fig. 4.2. I show the relaxation of the profile in Fig. 4.1 a) because it has a very steep gradient, which makes the relaxation effect more pronounced and easier to see.)

Now, rather than developing a first principle's source based on the theoretical source/sink expressions, I use ad hoc controlling sources. I estimate that $\langle N_t \rangle_{fs}$ remains constant over time, and model the source using the integral portion of a PID controller. This means that I write an equation for the source:

$$\partial_t S_n = - \langle N \rangle_{fs}. \tag{4.5}$$

Therefore,
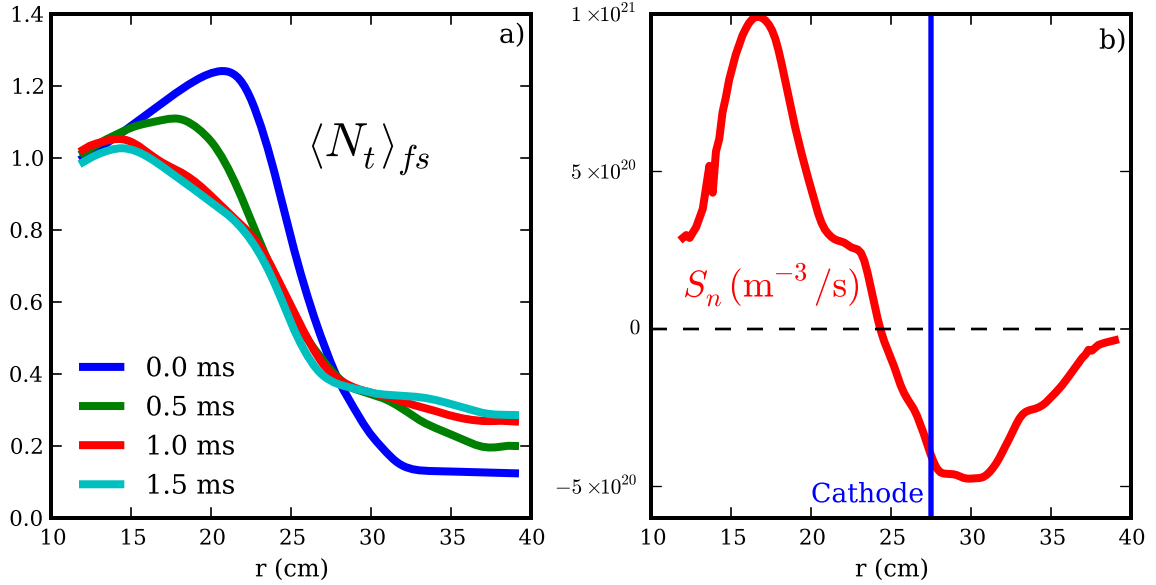
Figure 4.1: a) Profile relaxation and b) evolved density source

$$S_n(t) = -\int_0^t \langle N(\tau) \rangle_{fs} \, d\tau. \tag{4.6}$$

A typical time-averaged density source is shown in Fig. 4.1 b). The upshot of using such a source is that $\langle N_t(t) \rangle_{fs} \simeq N_0$. Notice that the source in Fig. 4.1 b) is net positive inside of the cathode radius and negative outside of it, just as one would expect. I use the same method for the temperature source. The temperature source ultimately comes from the hot electrons that are boiled off of the cathode, which transfer their energy to the plasma through ionizing collisions. This heat transfer is mostly to the electrons of the plasma. The temperature sink is caused by collisions with ions and neutrals which line radiate and by heat loss to the sheath and end walls.

I emphasize that the sources are not first principle sources. They are constructed based on the simulated radial transport. The alternative first principle's approach was used by Rogers and Ricci for LAPD [RR10]. They use a stationary

top-hat-like ionization source that models the physical density-producing process in LAPD. Furthermore, they do not separate equilibrium from fluctuations or input equilibrium profiles. Their source feeds the density, which then transports itself until it comes to a quasi-equilibrium state (a sink is also present). This method solves for the full plasma state with very little experimental input. They input the sources and derive the plasma state. On the other hand, I input part of the plasma state and derive the sources. As stated before, our method has the advantage of using experimentally measured profiles. This experimental input allows us to more easily simulate turbulence that resembles that in the experiment, and therefore make conclusions on the fluctuation properties. I do not, however, evolve the equilibrium and gain the knowledge that comes from that.

4.1.2 Artificial Diffusion and Viscosity

Artificial diffusion or hyperdiffusion terms are ubiquitous in fluid simulations. They are generally intended to prevent high frequency or high wavenumber ringing caused by numerical advection schemes at steep interfaces. They can, however, cause unphysical smoothing in systems that are non-diffusive and non-viscous or cause over-smoothing if applied haphazardly. Some numerical advection schemes contain their own diffusion, called numerical diffusion. Other non-advective finite difference schemes also contain numerical diffusion or dispersion.

I use artificial diffusion and viscosity for several reasons. The first is to prevent artificial high-wavenumber oscillations due to the Arakawa advection scheme that I use [Ara66]. Second, it smooths out the solutions, preventing the total density and temperature from becoming negative at any point in space, which is obviously unphysical. Third, I can use it to prevent the need to go to very fine grid spacing at which physical diffusion and viscosity are important. Finally, I can use it to help saturate the turbulence at levels consistent with experiment. These reasons are all somewhat related, and more discussion is left to Appendix B.

Diffusion and viscosity are real effects that are present in the non-reduced Braginskii equations. In Chapter 3, I made the approximation that $\nabla \cdot (n\mathbf{v}_{\perp e}) = \mathbf{v}_E \cdot \nabla n$, which neglected the polarization velocity part of $\mathbf{v}_{\perp e}$. Now the "full polarization velocity" [SC03] (from crossing Eq. 3.3 with $\mathbf{b}$ and neglecting the stress tensor) is

$$\mathbf{v}_{pe} = (1/\omega_{ce}) \left[\frac{d(\mathbf{b} \times \mathbf{v}_{\perp e})}{dt} + \nu_e \mathbf{b} \times \mathbf{v}_{\perp e} - \nu_e \mathbf{b} \times \mathbf{v}_{\perp i} - \frac{3}{2} \frac{\nu_e}{m_e \omega_{ce}} \nabla_{\perp} T_e \right]. \quad (4.7)$$

The part of this that causes collisional diffusive terms is $(\nu_e/\omega_{ce})\mathbf{b} \times \mathbf{v}_{\perp e}$. Now this contains $\mathbf{v}_{\perp e}$ itself, which must be approximated as $\mathbf{v}_{\perp e} = \mathbf{v}_E + \mathbf{v}_{de}$ to allow for closure. Only the diamagnetic drift part will be important for the collisional diffusion, so the part of the polarization velocity that I focus on is $(\nu_e/\omega_{ce})\mathbf{b} \times \mathbf{v}_{de}$. Recall that I want to use this in the continuity equation, so I am interested in the term $\nabla \cdot (n_e v_e) \rightarrow \nabla \cdot (n_e(\nu_e/\omega_{ce})\mathbf{b} \times \mathbf{v}_{de}) = -\nabla \cdot \frac{\nu_e m_e}{e^2 B^2} \nabla_{\perp} p_e$. Now defining $D = \frac{\nu_e m_e T_e}{e^2 B^2}$, I have $\nabla \cdot (n_e v_e) = -\nabla \cdot (D\nabla_{\perp} n)+$ lots of other terms. D is the classical diffusion coefficient, which is about $0.01\text{m}^2/\text{s}$ for LAPD parameters. One of the terms in $\nabla \cdot (D\nabla_{\perp} n)$ is $D\nabla_{\perp}^2 n$, which has the same form of the artificial diffusion term that I've added to Eq. 4.1. Of course, I have neglected many terms of the same order as this term in Eq. 4.1, but this shows that such a classical diffusion term is present in the Braginskii equations.

A similar treatment can be used for the energy conservation equation (Eq. 3.6), using the same procedure as for the continuity equation but with the $p_e \nabla \cdot \mathbf{v}_e$ term in Eq. 3.6. The result is $p_e \nabla \cdot \mathbf{v}_e = Dn_e \nabla_{\perp}^2 T_e+$ lots of other terms. This has the same form as the temperature diffusion term in Eq. 4.4.

The viscosity in the vorticity equation comes from the ion stress tensor term $\frac{\partial \Pi_{i\alpha\beta}}{\partial x_{\beta}}$ that I neglected when deriving the vorticity equation because I neglected everything with finite ion temperature. If this was included, a vorticity diffusion term (aka a viscosity) would have been included in the vorticity equation [PUC10b]

as it is in other equation sets like the well-known Hasagawa-Wakatani equations [HW83]. The magnetized Braginskii viscosity coefficient is $\eta_1^i = \frac{3nT_i}{10\omega_{ci}^2\tau_i}$, which is about $2 \times 10^{-8}\mathrm{kg/m \cdot s}$ for LAPD. Since LAPD's ions are not necessarily magnetized due to the fact that $\omega_{ci}\tau_i \sim 1$, the unmagnetized ion viscosity is $\eta_0^i = 0.96nT_i\tau_i$ [Bra65] which is about $4 \times 10^{-7}\mathrm{kg/m \cdot s}$.

For the artificial diffusion and viscosity coefficients in Eqs. 4.1-4.4, I use a single value of 1.25×10^{-3} in our normalized units, which is $0.075\mathrm{m^2/s}$ in real units. I find that this value produces turbulent fluctuation levels consistent with experimental levels. I use this as a free parameter in this sense. This value is much larger than the real classical diffusion D, but is smaller than $\frac{\eta_1^i}{nm_i} = 1\mathrm{m^2/s}$. Nevertheless, I neglected a number of terms in Eqs. 4.1-4.4 such that there isn't justification to use the real diffusion and viscosity in these equations. Artificial diffusion and viscosity terms, however, serve a numerical purpose.

4.2 Boundary Conditions

Boundary conditions are often difficult to determine in plasma devices. While the properties of the boundaries are usually known, the way that the plasma interacts with them can be complex. Plasma boundary physics is one of the main elements of present day fusion research [Sta00]. Often times there is uncertainty in the equations that need to be used in simulations, and once the equations are found, they can be difficult to implement in codes.

The boundary conditions in LAPD are difficult to determine. LAPD contains at one end, a hot emitting cathode behind a biased mesh annode. In front of the annode are biasable azimuthal limiters with radius about equal to the cathode radius, though the limiter radius may be changed. The far end contains a floating mesh plate. The cylinder is conducting and has a radius about 20 cm larger than the cathode radius.

4.2.1 Simple Boundaries

In all simulations, I use an annulus rather than a cylinder. Although the inner radius of the annulus may be arbitrarily small, I take the inner radius to be 12 cm. I take the outer radius to be 39 cm. This is generally the radial extent of our experimental probe measurements. Furthermore, the plasma fluctuations are nearly zero (when normalized to values at the cylindrical axis) outside of this annular region, which is seen in Fig. 3.1 c). Therefore, I set the radial boundaries on all of the fluctuating variables ($N, \phi, v_{\parallel e}$, and T_e) to zero. It would be nice in the future to take data spanning at least a few more cm and extend the simulation domain accordingly. But for now, the results use such an annular domain.

As for the axial boundaries, I use four different boundary conditions: periodic, zero-value (Dirichlet), zero-derivative (Neumann), and Bohm sheath. The only non-trivial one, Bohm sheath, is derived and described in the following subsection. The others are all trivial to implement and provide a test of the importance of the axial boundary conditions on the nature of the turbulence.

4.2.2 Bohm Sheath Boundaries

Bohm sheath boundary conditions are applicable when a plasma terminates at a conducting plate. I note that this is not necessarily the case in LAPD. The cathode/annode system is obviously much different from a simple floating or biased conducting plate. Furthermore, the mesh wall at the far end is not a solid wall. Moreover, it's not clear if the plasma is even attached to the far end mesh wall or if it becomes detached in the neutrals in front of it, where the plasma cools and recombines before interacting with the wall. In any case, it is still instructive to apply such an idealized boundary condition to LAPD because it is somewhat more realistic than the simpler boundary conditions, and it creates a new linear instability (see Sec. 5.1.2), which can be used to test the robustness of LAPD's

nonlinear instability. Therefore, I proceed with the derivation of the Bohm sheath boundary conditions.

Now, it is known that to good approximation, a plasma bounded by a wall can be divided into two regions: the main plasma and the Debye sheath [Sta00]. The Debye sheath is a small region adjacent to the wall, generally several Debye lengths long. It has a net positive charge $(n_i > n_e)$ that shields the negative charge on the wall. The sheath does not completely shield the negative wall, however, and a small electric field penetrates into the main plasma (the ambipolar field), which mostly serves to accelerate the cold ions toward the wall, and slightly retard the electrons before entering the sheath. In the main plasma, the quasi-neutrality relation holds $(n_i = n_e)$.

The well-known Bohm criterion along with other considerations restricts the ions to move into the sheath entrance at the sound speed $c_s = \sqrt{T_e/m_i}$. I consider here the case where there is no external biasing; in other words, the end plates are electrically isolated and floating. The wall can be set to an arbitrary potential, say $\phi_w = 0$, while the potential at the sheath entrance is then the positive floating potential ϕ_{sf}. This potential difference across the sheath reflects slow electrons that enter the sheath. The electrons approximately maintain a cutoff Maxwellian velocity distrubution throughout the sheath, and at the wall, their velocity is retarded by a Boltzmann factor due to the floating potential. In total, the current to the wall is [BRT91, BCR93, XRD93]

$$J_\parallel = \pm en \left[c_s - \frac{(T_e/m_e)^{1/2}}{2\sqrt{\pi}} e^{\left(-\frac{e\phi_{sf}}{T_e}\right)} \right], \qquad (4.8)$$

where the $\pm$ indicates that the plasma flux goes into the wall, which is in different directions for the different end plates. Note that there is a factor of $\sqrt{2}$ discrepancy between different reports on the expression used for the thermal velocity, which should have only a minor consequence. In this expression, all

values are total (equilibrium + fluctuations).

Now, this is not only the current to the wall, but also the current going into the sheath edge, since the sheath is too small for there to be appreciable radial current loss or an ionization source within the sheath. All values, in fact, are taken to be those at the sheath edge. Furthermore, since the wall is electrically isolated, the equilibrium current at the wall vanishes. This sets the value for the floating potential to be $\phi_{sf} = \Lambda T_{e0}/e$ with $\Lambda = \ln\left(\frac{1}{2\sqrt{\pi}}\sqrt{\frac{m_i}{m_e}}\right)$. Note that T_{e0} is a function of radius, meaning ϕ_{sf} is also a function of radius. Thus, a radial temperature gradient produces a radial electric field, at least at the sheath edge and likely penetrating axially into the main plasma. It is noted that $J_\parallel$ need not vanish on every field line since the end plates are conducting and charges can move around on the plate, however, the vanishing equilibrium current is generally a fair approximation [BCR93].

On the other hand, the fluctuating component of the current is allowed to vary between field lines. The first order fluctuating component is obtained by linearizing Eq. 4.8, giving the result:

$$J_\parallel = \pm eN_0 c_{s0}\left[\frac{e\phi}{T_{e0}} - \Lambda\frac{T_e}{T_{e0}}\right],\tag{4.9}$$

where now, $J_\parallel, \phi$ and T_e are fluctuating components, consistent with previous notation. This expression for the current sets the fluctuating axial boundary condition of the plasma and is often called the Bohm Sheath boundary condition. This current condition holds both at the wall and at the sheath entrance. So rather than taking the simulation domain all the way to the wall, simulations often end at the sheath entrance and employ this analytically derived boundary condition to the boundaries of the main plasma. Then one doesn't have to worry about the small spatial scales and the non-quasineutrality of the sheath. The corresponding boundary conditions for the other fluid variables such as the density

and temperature have recently been derived by Loizu et al. [LRH12]. However, I simply take them to have zero-gradient as most others have done, although this isn't wholly inconsistent with Loizu's calculations.

Now while one may set the parallel current (or equivalently $v_{\|e}$) at the axial boundaries to the quantity on the right hand side of Eq. 4.9, I don't do that. I use Ohm's Law $(-\nabla_{\|}\phi = \eta_{\|}J_{\|})$ to set the boundary condition for the gradient of ϕ. I do this for practical reasons in the coding. Therefore, the boundary condition used in the code is (in our normalized units):

$$\nabla_{\|}\phi = \pm \frac{\nu_e m_e}{m_i}\left(\phi - \Lambda T_e\right).$$ (4.10)
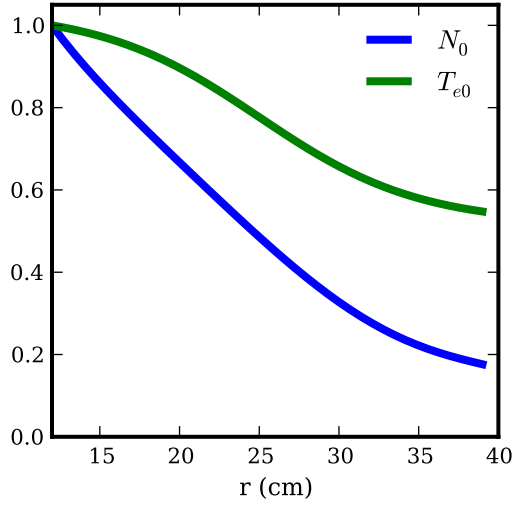
4.3 Profiles and Parameters

Figure 4.2: Equilibrium density and electron temperature profiles

As explained above, I take all equilibrium profiles and parameters from experimental measurements. All simulations before Chapter 9 use profiles and parameters from one particular experiment. This experiment used limiter biasing to

essentially null out the mean radial electric field [SCR12]. I used this experiment so that I could neglect the mean potential profile in the equations (as is done in Eqs. 4.1-4.4), which simplifies our analysis. The normalized profiles that I use are shown in Fig. 4.2, and the parameters are shown in Table 4.3. The density profile is a polynomial fit to the experimental equilibrium density profile. The temperature profile is a tanh function that somewhat resembles typical LAPD temperature profiles. At the time of the first simulations, I didn't have reliable temperature profile measurements, so I was forced to estimate what the profile might look like. I note that the real temperature profile has a steeper gradient than the one I use. And again, I use $\phi_0 = 0$, which is a good approximation for the experimental nulled out potential profile.

The profiles that I use have no azimuthal or axial variation because I don't have the corresponding experimental measurements. So I assume that the equilibrium profiles are only functions of radius. It's likely, however, that there is some axial variation in the profiles and parameters. In LAPD, $\nu^* \equiv L_\parallel/\lambda_{ei} \sim 100$, generally indicating that a parallel temperature gradient can exist depending on the locations of the sources and sinks [Sta00]. Furthermore, if the Bohm sheath boundary condition is correct, the equilibrium potential must have a parallel gradient in order to accelerate the ions up to the sound speed at the sheath entrance. This ambipolar parallel electric field should exist between the location of the sheath entrance and an ion collision length into the main plasma. The parallel electric field generated by the condition of Eq. 4.10 is just the perturbed field that responds to electron temperature perturbations. It doesn't constitute the equilibrium electric field.

Moreover, recall that the Bohm sheath condition combined with a radial equilibrium electron temperature profile implies (at least near the sheath) a corresponding equilibrium potential profile, since $\phi_{sf} = \Lambda T_{e0}/e$. Experimentally, this relation doesn't hold where the plasma is measured, meaning that either the am-

bipolar field doesn't penetrate far into the plasma or that the real LAPD boundary conditions are more complicated than simple floating conducting plates. So I don't use any equilibrium axial variation, leaving this to future work.

Species	^{4}He
Z	1
n	2.86×10^{18} m^{-3}
T_e	6 eV
T_i	$\lesssim 1$ eV
B_0	0.1 T
$L_\parallel$	17 m
a	0.4 m
λ_D	10^{-5} m
ω_{ci}	2.4×10^6 rad/s
ω_{ce}	1.8×10^{10} rad/s
ρ_e	5.3×10^{-5} m
ρ_i	$\sim 1 \times 10^{-3}$ m
ρ_s	5×10^{-3} m
v_{te}	9.4×10^5 m/s
c_s	1.1×10^4 m/s
v_A	7×10^5 m/s
β	5×10^{-4}
m_e/m_i	1.4×10^{-4}
$\ln\Lambda$	11
ν_e	7.2×10^6 Hz
λ_{ei}	0.13 m
ν_i	$\sim 10^6$ Hz
ν_{in}	3×10^3 Hz
$\kappa_\parallel^e$	9.8×10^{23} eV/m^2 s
η_0^i	$\sim 10^{12}$ eV s/m^3
ω_*	$\sim 5 \times 10^4$ rad/s

Table 4.1: LAPD simulation parameters

CHAPTER 5

The Nature of LAPD Turbulence

Simulations can supplement experiment by providing detailed spatial data that is too difficult to obtain experimentally. This spatial data can be analyzed, revealing new properties of the experiment. In order for simulations to provide information, however, they must accurately represent the system which they model. Assessing the validity of simulations generally comes in two parts: verification and validation. Verification, the evidence that the code solves the equations correctly, will not be taken up here. I note, however, that my collaborators and I have done verification studies in the past, somewhat detailed in Popovich et al. [PUC10a]. We compared linear BOUT (the old version of BOUT++) and BOUT++ simulations to analytic solutions as well as to eigensystem solver solutions. On the other hand, I will focus parts of this chapter on our validation effort. Validation is the evidence that the simulation model accurately reproduces features of the experiment. Generally, the more features of the experiment that the model reproduces, the more valid the model. While this chapter focuses on simple analyses to describe the nature of the simulated turbulence, it will also make comparisons, where possible, to experimental data in order to show that the model is relatively well validated. First, however, I analyze the linear instabilities in the LAPD simulations, and this affords no experimental comparison.

5.1 LAPD Linear Instabilities

Linear instabilities are prevalent in plasma physics. They come from the linearization around an equilibrium of the plasma equations. Physically, if a plasma is in a time-independent steady state that is linearly unstable and a finite fluctuation of any size occurs, the fluctuation will grow exponentially. Linear instabilities often drive hydrodynamic and plasma turbulence. I therefore study the linear instabilities of the LAPD system before moving onto the turbulence because they can offer insight into the nature of the turbulence. The LAPD equations, parameters, and profiles described in Chapter 4 give rise to a couple of linear instabilities. They are both drift wave type instabilities, but they have different pressure/potential coupling mechanisms. One type couples through the adiabatic response, while the other couples through the sheath boundary response.

5.1.1 Drift Waves

Electron drift waves driven by an equilibrium density or pressure gradient that use the adiabatic response are generally referred to as just drift waves or the universal instability. The electron drift wave mechanism is the following: An electron pressure fluctuation in the plasma is linked with a potential fluctuation through the adiabatic response. The adiabatic response is simply a parallel force balance between the pressure force and the electrostatic force. A simplified version of Eq. 3.3 can be written:

$$\nabla_\parallel p_e = en\nabla_\parallel \phi + Rv_{\parallel e}, \tag{5.1}$$

where the term $Rv_{\parallel e}$ represents effects such as electron inertia, resistivity, and electromagnetic induction. If $R = 0$, the electrons are said to be adiabatic, meaning $\nabla_\parallel p_e = en\nabla_\parallel \phi$. When T_e fluctuations are neglected and $\nabla_\parallel \neq 0$, this integrates to the Boltzmann expression:

$$n = n_0 e^{e\phi/T_e}. \qquad (5.2)$$

For any R and T_e fluctuations, the parallel electron dynamics couple the pressure to the potential as long as the parallel wavelength $k_\parallel$ is finite. The perpendicular electric field associated with the potential fluctuation has a component in the azimuthal direction with $k_\perp \gg k_\parallel$. This creates a radial $\mathbf{E} \times \mathbf{B}$ drift that advects the pressure in the radial direction. Because of the radial pressure gradient, the fluctuation to propagates azimuthally as a wave at the drift speed $v_{De} = \frac{T_e}{eB} \frac{\partial \ln N_0}{\partial r}$ [Che06] in the electron diamagnetic drift direction. If there is a small phase difference between the pressure and the potential of the wave (the result of $R \neq 0$), the equilibrium pressure gradient will enhance the fluctuation, causing instability. Since $p_e = n_e T_e$, the pressure fluctuation may be due to either a density fluctuation, an electron temperature fluctuation, or both. The universal instability generally refers to the situation where an equilibrium density gradient drives a density fluctuating wave. But a temperature gradient driving a temperature fluctuation wave is also possible, and may be called a thermal drift wave [MTK11]. It's not necessary, however, to separate them, and I will just refer to both of these as drift waves.

The LAPD equation set (Eqs. 4.1-4.4) supports such drift waves, which are unstable with the parameters and profiles used in the simulations. The growth rate as a function of the azimuthal wavenumber m is shown in Fig. 5.1 a) for the LAPD parameters in Table 4.3 and profiles in Fig. 4.2. The growth rates are found by simulating the linearized version of Eqs. 4.1-4.4 in BOUT++ with the three different simple axial boundary conditions: periodic, zero-value (Dirichlet), and zero-derivative (Neumann). The linear equations simply omit the advective nonlinearities and the source terms, though the source terms have no affect on any of the linear modes besides $m = 0$ modes. The simulations are run for long enough so that the fastest growing modes can dominate the dynamics.
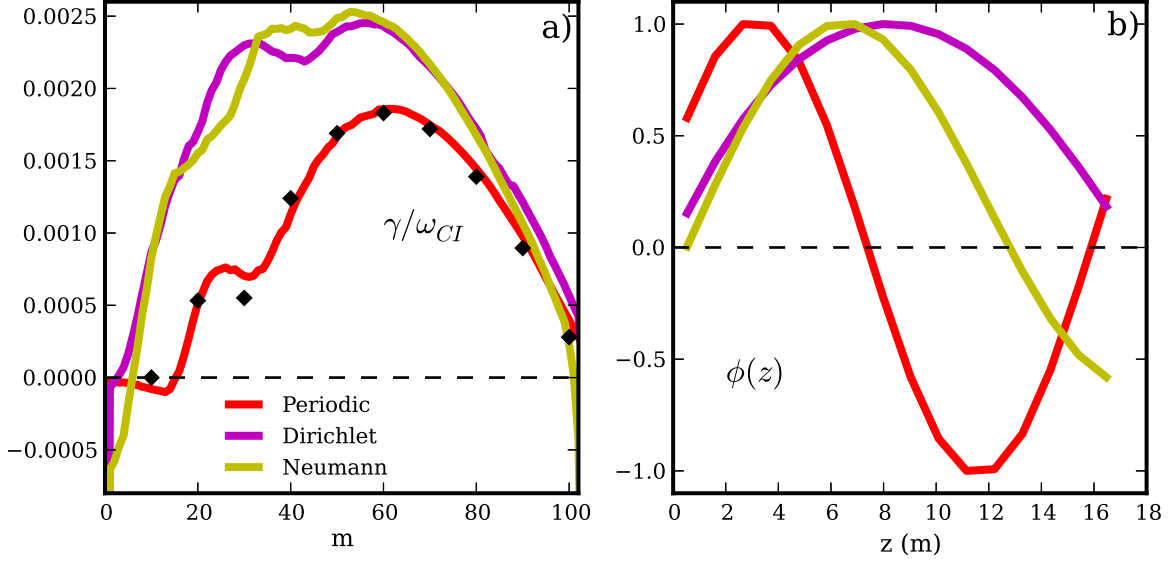
Figure 5.1: Linear drift wave a) growth rates and b) axial structures

The solid curves in Fig. 5.1 are calculated from the simulation results using the formula, $\gamma_m = \frac{\partial E_m}{\partial t}/(2E_m)$ where E_m is the energy of the fastest growing linear eigenmode with azimuthal mode number m. The energy is defined in Chapter 6. The details of obtaining γ_m are explained in that chapter, but for now, it is sufficient to state that this procedure calculates γ_m at a particular time using only the structures of the fluctuating quantities: $N, \phi, v_{\parallel e}$, and T_e. An alternative way to calculate γ_m is to use BOUT++'s Fourier filtering capabilities and run many simulations where each one filters out a different azimuthal mode. Then, I take the log of the envelope of one or several of the fluctuating quantities and calculate the slope of the line, which gives the growth rate for each particular simulation. This procedure uses the time signal of the fluctuations rather than their spatial structure to calculate the growth rate, thus providing a check on the first method. The results using this alternative method for the periodic case are shown with the black diamonds in Fig. 5.1 a), which agree well with the curve calculated using the alternative energetic structure-based calculation. I do this

33

check with all of the simulations to ensure consistency. This second method is more time consuming, so I only sample a few values of m. Furthermore, it's difficult to get growth rates when $\gamma_m < 0$ using this second method.

The difference in the growth rate curves with the different boundary conditions is due to the different $k_\parallel = \frac{2\pi n}{L_\parallel}$ where n is the axial mode number. The periodic simulation restricts n to integer values, while the Dirichlet and Neumann simulations allow for any fractional n. The largest growth rate occurs for $n \sim 1/2$. The Dirichlet and Neumann axial structures for the most unstable m mode, shown in Fig. 5.1 b), reflect this. The periodic simulation, which has $n = 1$ structure, has a smaller growth rate, especially at low m. Note that in Fig. 5.1 b), the axial boundaries are not plotted. For instance, the zero-valued boundaries for the Dirichlet simulation are not shown. Also, the axial structures are taken at one random point in the $r - \theta$ plane and at one time point, and are normalized to their maximum value.

5.1.2 Conducting Wall Mode

I now consider the linear instability that can exist in a plasma bounded by two conducting walls on the boundaries where the magnetic field lines terminate (the axial boundaries) [BRT91, BCR93, XRD93]. The instability is actually of the drift wave variety, but unlike the drift waves discussed above, the pressure-potential coupling mechanism is through the sheath boundary response rather than through the adiabatic response. The Bohm sheath boundary conditions that were derived in Sec. 4.2.2 can provide this coupling. As already noted, these boundary conditions are not necessarily the correct ones for LAPD, but are somewhat idealized. Yet, it is still academically instructive to apply such an idealized boundary condition to LAPD because it creates this new linear instability, which can be used to test the robustness of LAPD's nonlinear instability.
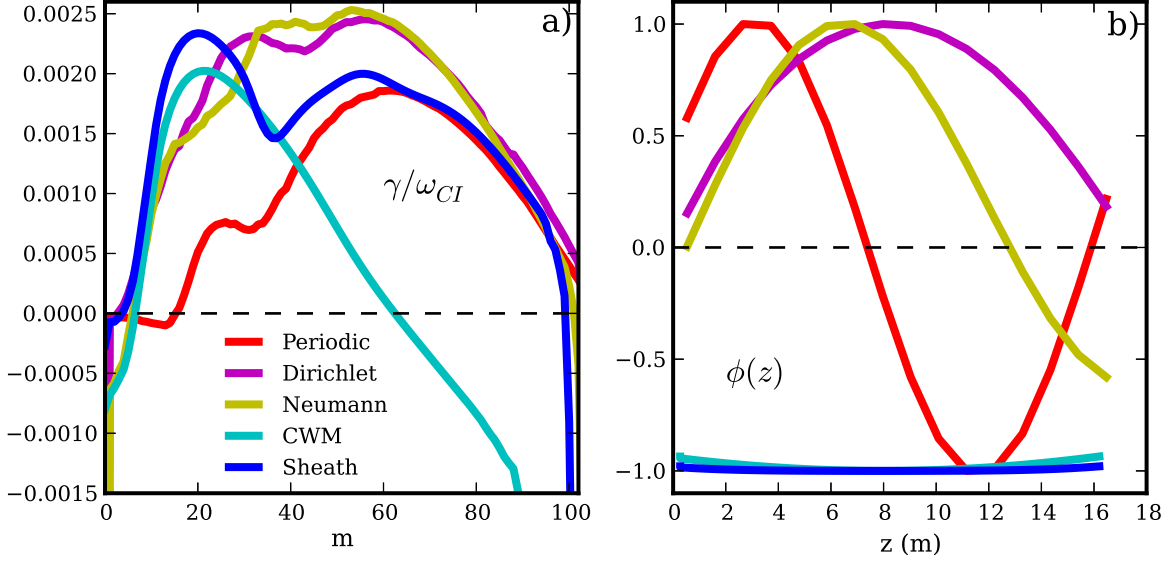
Figure 5.2: Linear conducting wall mode a) growth rates and b) axial structures

The conducting wall mode (CWM) instability in the case considered here is purely an electron temperature gradient instability, although other types of gradients can cause it [BCR93]. Electron temperature fluctuations are advected by electrostatic potential fluctuations and feed off the equilibrium electron temperature gradient as in the case of the thermal drift waves. However, in contrast to the thermal drift waves, the coupling between the temperature and potential fluctuations comes through the sheath boundary condition rather than through the adiabatic response. Furthermore, the CWM can have (nearly) $k_\parallel = 0$ flute-like behavior. The coupling mechanism is as follows: an electron temperature perturbation – say a positive constant fluctuation along a small flux tube – increases the sound speed and the electron thermal speed on the flux tube. Since the ions must enter the Bohm sheath at the sound speed by being accelerated by a parallel electric field, the temperature increase must coincide with an increase in the parallel potential gradient as derived in Eq. 4.10. Additionally, the increased electron thermal speed causes an increase in the floating potential along the flux

tube. These serve to couple the electron temperature to the potential.

The CWM can be isolated from the normal drift waves by removing the adiabatic response from the full LAPD equation set, and of course using the Bohm sheath boundary condition of Eq. 4.10. Removal of the adiabatic response in this case means removal of the $\nabla_{\|}p_e$ and the $0.71\nabla_{\|}T_e$ terms in the parallel momentum equation (Eq. 4.2). This causes the density fluctuation N to become a passive scalar, so Eq. 4.1 can be removed as well with no consequence. So the isolated linear CWM equations are:

$$\partial_t v_{\|e} = \frac{m_i}{m_e}\nabla_{\|}\phi - \nu_e v_{\|e}, \tag{5.3}$$

$$\partial_t \varpi = -N_0 \nabla_{\|} v_{\|e} - \nu_{in}\varpi + \mu_\phi \nabla_\perp^2 \varpi, \tag{5.4}$$

$$\partial_t T_e = -\mathbf{v_E} \cdot \nabla T_{e0} + \frac{2}{3N_0}\kappa_{\|e}\nabla_{\|}^2 T_e - \frac{2m_e}{m_i}\nu_e T_e + \mu_T \nabla_\perp^2 T_e, \tag{5.5}$$

The CWM growth rate curve is shown in Fig. 5.2 a). The CWM is most unstable at values of $m \sim 20$, which is much lower than the $m \sim 60$ values of the drift waves. Furthermore, the CWM maximum growth rate is about equal to the drift wave growth rates. And from Fig. 5.2 b), the CWM axial structure is flute-like ($k_{\|} \simeq 0$). Finally, the growth rate curve of the full set of equations along with the sheath boundary condition is shown in this figure as the curve labeled "sheath." This set of equations contains the drift wave and CWM instabilities. From both Figs. 5.2 a) and b), it is clear that the sheath simulation is dominated by the CWM at $m \leq 20$, which in fact is where the growth rate is maximum. At $m \geq 40$, the drift waves dominate.

5.2 LAPD Turbulence: A Visual Examination

When I simulate the full LAPD equation set with the advective nonlinearities and source terms, I find that the simulation develops into a turbulent state. To
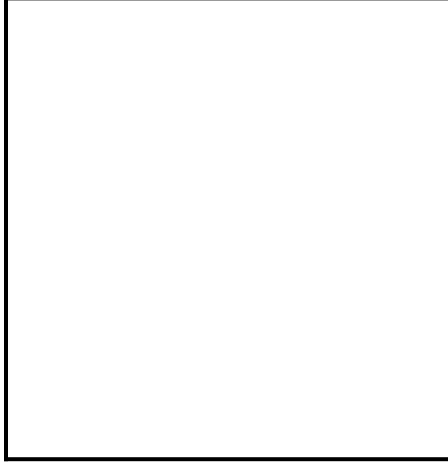
Figure 5.3: 3D turbulent simulation animation

start the simulation, I initialize each fluctuation quantity ($N, \phi, v_{\parallel e}$, and T_e) with a small random 3D spatial structure. The structure evolves and a coherent structure emerges (the fastest growing linear eigenvector), which grows exponentially in time. Once the normalized fluctuations reach values on the order of $0.01-0.1$, they saturate and appear to be turbulent. A 3D animation of the density fluctuation N is shown in Fig. 5.3. The animation shows a 1/8th wedge of the simulated annulus to make the axial extent of the annulus visible. The animation begins right before the fastest growing mode structure becomes dominant. The fastest growing mode dominates the structure for some time, where there is a clear coherent wave structure that simply propagates in the electron diamagnetic drift direction. This stage is called the linear stage since the linear terms in the equations dominate the evolution. Note that the axial structure in the linear stage has a finite wavelength about half of the length of the animation domain. The axial boundary conditions used here (Neumann) allow for such a structure.

Soon, the coherent eigenmode structure, which has been growing in magnitude, saturates and transitions to a turbulent-looking state that I call the turbulent

stage. The evolution of the RMS fluctuation amplitude of the density and potential is shown in Fig. 5.4 a). The potential is separated into a flux-surface-averaged component ϕ_{fs} and the remainder $\phi - \phi_{fs}$. ϕ_{fs} quantifies the amplitude in the zonal flow, which appears in Fig. 5.4 a) to possibly have some role in the initial saturation, but has a relatively small magnitude in the turbulent stage. For all the fluctuations, the exponential growth period during the linear stage is followed by saturation corresponding to the visual change from coherent to turbulent spatial structures in the animation. Upon transition to the turbulent stage, I notice in the animation that there is also a qualitative change in the axial mode structure. The axial structures elongate, looking more flute-like than in the linear stage. I confirm this by taking the axial Fourier transform of the density fluctuations and plotting the RMS values of the different axial mode numbers in Fig. 5.4 b). The linear stage is dominated by the $n = 1$ Fourier component, while the turbulent stage is dominated by the $n = 0$ flute mode component. I found this to be an interesting and unexpected transition when I first identified it. There is not only the expected bifurcation from linear waves to turbulence, but also the unexpected bifurcation from linear drift wave structures to turblent flute-like structures. I will discuss why this is unexpected in the upcoming chapters, and I will show in detail what causes it. But take note that this is a key finding. This $n = 0$ dominance in the turbulent stage is the main subject of the remaining chapters.

However, before I jump into the analysis of the $n = 0$ mode dominance, I continue to look at simple and common turbulence analysis techniques to describe the nature of the turbulence and to validate the simulations. Continuing on with the visual examination, I show one visual comparison between the simulation and experiment. For the experimental visual, I use a processed fast camera movie. The camera records the light intensity given off by the plasma. The light is primarily due to line radiation of the helium atoms and ions. It should be some function of plasma density, neutral density, and plasma temperature. Noting that the
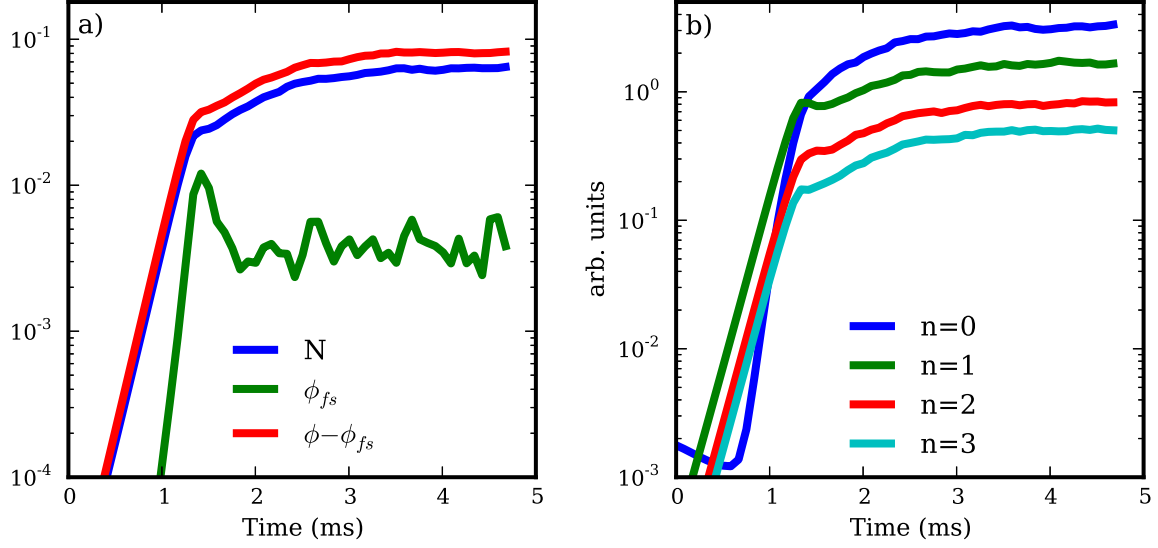
Figure 5.4: RMS time evolution of a) fluctuations and b) axial mode numbers

comparison is certainly not exact, I show the experimental camera data next to corresponding simulation data of the density N signal during the turbulent stage. This is shown in Fig. 5.5. The animations cover the same spatial domain and last for equal time intervals (about 2 ms). Both are simply fluctuation data with the time-independent background not included (subtracted out from the camera data).

Visual comparisons like this are certainly not quantitative, and at best this comparison reveals that both simulatin and experiment appear turbulent and contain similarly sized spatial structures and similar time scales. The camera data can be a valuable tool since it provides so much simultaneous spatial data – something that is difficult to do with probes. Nevertheless, I do not proceed here with detailed statistical analysis of the camera data or any quantitative comparisons between the camera and simulation. This work is left for future studies. Rather, I now focus on statistical analysis of the simulation data, and compare it to experimental Langmuir probe data when possible.

a) Simulation   b) Experiment
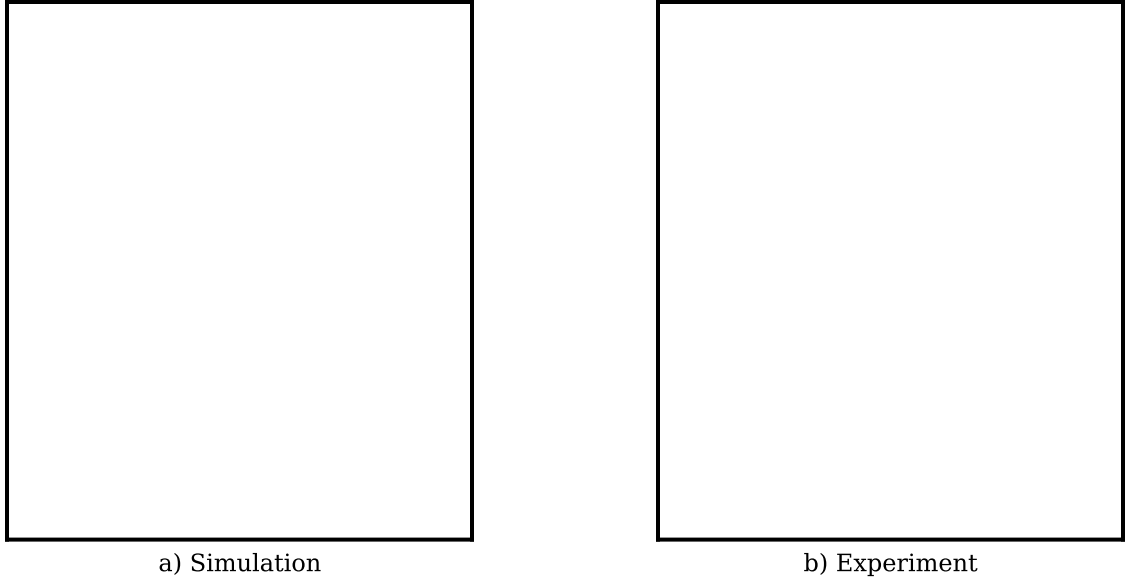
Figure 5.5: Turbulent movies

5.3 LAPD Turbulence: A Statistical Examination

Stochastic turbulent systems or even chaotic systems with relatively few degrees of freedom that are subject to external fluctuations do not have predictable phase space states for long time periods. These systems do, however, have reproducible average properties. It's therefore useful to look at time series and spatial states of such systems in a statistical way. Turbulence in plasmas, in fact, is often characterized by statistical properties such as spectra, pdfs, and spatial and temporal correlations. Furthermore, statistical data can be extracted from both simulations and experiment in similar ways, which can then be used to validate simulations.

5.3.1 Experimental Probe Data

There are many different kinds of experimental measurements, but I focus here only on Langmuir probe measurements. The Langmuir probes in LAPD generally

provide time series data although I do have some two-probe data that provides certain spatial information. Langmuir probes do not directly measure any of the independent state or flux variables of the simulation $(N, \phi, v_{\parallel e}, T_e)$, but they can measure quantities that are functions of these variables. The probes are biased to a known potential (with respect to a reference like the cathode potential), and the current they draw from the plasma is measured. As long as the probes are biased sufficiently below the plasma potential so as to repel most electrons, they develop sheaths around them in the same way as the conducting plates considered in Sec. 4.2.2. The ion current to the probe is [Hut02]

$$I_i \sim \frac{1}{2} e A_s n c_s \qquad (5.6)$$

where A_s is the sheath area, approximately equal to the probe area, and the factor of $\frac{1}{2}n$ is the reduction of density at the sheath edge compared to the main plasma. The probe may be biased negatively enough so that all electrons are repelled. The current collected is just that of Eq. 5.6, called the ion saturation current. As the probe voltage is swept positively from this point, more electrons are collected. The total current to the probe then takes the form [Hut02]

$$I = e A_s n c_s \left[\frac{1}{2} - \left(\frac{m_i}{2\pi m_e} \right)^{1/2} e^{eV_p/T_e} \right], \qquad (5.7)$$

where V_p (which is negative) is the potential of the probe with respect to the plasma potential. When $I = 0$, the probe potential is at the floating potential: $\frac{e(V_f - \phi)}{T_e} = \frac{1}{2} \ln \left(\frac{\pi m_e}{2 m_i} \right)$. The temperature can be obtained by sweeping the probe potential to get $\frac{\partial I}{\partial V_p}$, which is an exponential function of V_p. So the logarithm of this function produces a straight line. Then, the temperature is:

$$T_e = e(I - I_i) / \frac{\partial I}{\partial V_p}. \qquad (5.8)$$

41

Now the sweeping process is too slow to obtain temperature fluctuations. It's best used to obtain the equilibrium temperature profile. Since a single Langmuir probe doesn't give temperature fluctuations, it's impossible to find the exact density and potential fluctuations, N and ϕ. The probes only produce I_{sat} and V_f fluctuation data. Nevertheless, the simulations produce N, ϕ, and T_e fluctuations, which I can use to calculate the I_{sat} and V_f simulation values using the relations: $I_{sat} = \frac{1}{2}eA_s n c_s$ and $V_f = \phi + \frac{T_e}{2e}\ln\left(\frac{\pi m_e}{2m_i}\right)$. So rather than manipulating probe data to find the experimental N and ϕ fluctuations, I can use the simulation data to calculate experimentally-accessible quantities. The derived simulation quantities are called synthetic diagnostics. Synthetic diagnostics are model-dependent and they bind together some of the fundamental underlying data. For instance, two measurements (I_{sat} and V_f) comprise three fundamental state variables (N, ϕ, and T_e), so the synthetic diagnostics bind the temperature fluctuations to the density and potential fluctuations. Nevertheless, synthetic diagnostics provide a way to make apples-to-apples comparisons between simulation and experimental data.

I show in Fig. 5.6, a statistical comparison between I_{sat} and V_f fluctuations from simulation and experiment. The simulation uses the full nonlinear equation set along with Bohm sheath axial boundary conditions. I also show simulation statistics for N and ϕ fluctuations so that they may be compared to the simulation statistics of the synthetic I_{sat} and V_f respectively. Figs. 5.6 a) and b) compare the frequency spectra and radial RMS amplitudes of experimental and simulation I_{sat} fluctuations along with N fluctuations from the simulation. Figs. 5.6 c) and d) compare the same statistical properties, but this time of V_f fluctuations along with ϕ fluctuations from the simulation. The I_{sat} fluctuations from the simulation have nearly identical statistical properties as the N fluctuations because I_{sat} is proportional to density but only weakly dependent on temperature (square root dependence). V_f fluctuations are also somewhat similar to ϕ fluctuations, but to a lesser degree due to the large dependence of T_e on V_f. Furthermore, the
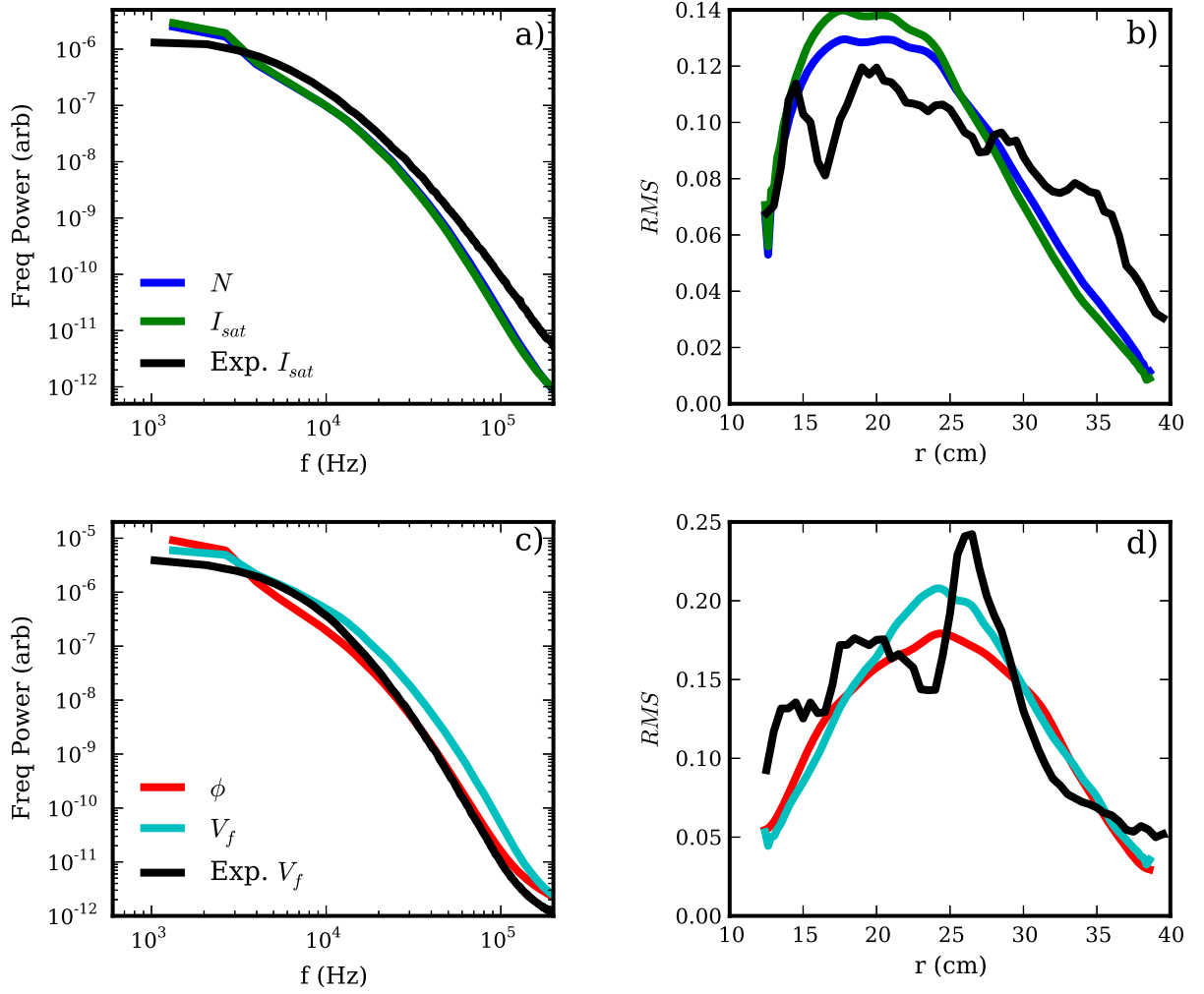
Figure 5.6: I_{sat} and V_f statistical data

simulation and experiment have very similar statistical properties, which I expand upon below.

5.3.2 Statistical Density Comparisons

A comparison of statistical properties of the experimental and simulation density fluctuations is shown in Fig. 5.7. I actually compare the N fluctuations for the

simulations to the I_{sat} fluctuations of the experiment, but as seen in Fig. 5.6, I_{sat} and N statistics are nearly identical. Fig. 5.7 contains results from five different simulations that all use the full nonlinear LAPD equation set (Eqs. 4.1-4.4) but differ in the axial boundary conditions as follows: 1) Periodic – uses periodic axial boundary conditions. 2) Sheath – uses Bohm sheath boundary conditions (Eq. 4.10). 3) $n = 0$ suppressed – uses axial boundary conditions, however, the axial average ($k_{\parallel}$ or $n = 0$) density, temperature, and potential fluctuation components are artifically removed from the simulation. 4) Dirichlet – uses zero-value axial boundary conditions. 5) Neumann – uses zero-first-derivative axial boundary conditions. I will discuss the $n = 0$ suppressed simulation more in Chapter 7, but for now it is sufficient to say that this simulation does not contain the nonlinear instability and is thus a control case by which to compare the others. It still contains the same linear instabilities as the Periodic simulation, however.

Fig. 5.7 a) shows the frequency power spectrum of the density fluctuations. I use a sliding Hamming window on the time series data and take the FFT, then take a volume average from 15 to 35 cm to get each simulation curve. I use the same technique for the experimental density fluctuation data, except I only have probe data at one location in the $\theta - z$ plane. The axial location is near the center of the machine. Fig. 5.7 b) shows the probability distribution function (PDF) of the density fluctuations, while Fig. 5.7 c) shows the RMS amplitude of the density fluctuations as a function of radius. Fig. 5.7 d) plots the radial k_r power spectrum of the simulations. I don't have experimental radial spectra data, which requires multiple probes at different radii. Fig. 5.7 e) is the azimuthal m_{θ} power spectra. Two probes separated azimuthally are used to obtain the experimental spectra. Finally Fig. 5.7 f) is the axial $k_{\parallel}$ spectra, and I don't have experimental axial spectra due to the difficulty of aligning two probes along a field line a significant distance from each other, which is required because of the long axial wavelengths of the modes.

Fig. 5.7 contains a lot of information about the simulations and experiment. The first obvious result is that the $n = 0$ suppressed simulation is statistically much different than all of the other simulations and the experiment. The density fluctuations of this simulation are a factor of 2-3 lower than that of the other simulations and the experiment. Furthermore, this simulation has peaks in the frequency, m_θ, and $k_\parallel$ spectra that are unique. The frequency and m_θ peaks are inconsistent with the experiment. Its spatial spectra peak at $m_\theta \sim 30$ and $k_\parallel \rho_s \sim 0.002 \rightarrow n = 1$, which is somewhat consistent with the linear growth rate spectra of Fig. 5.1, although the m_θ peak location is somewhat less than the maximum linear growth rate value of m_θ, which is around 60 when the axial boundaries are periodic. This differs significantly from all of the other simulations and the experiment which have peaks at $m_\theta \sim 10$ (if they peak at all). And again, as was clear from Fig. 5.4 b), all of the other simulations are strongly dominated by $n = 0$ axial mode numbers, which will be explained in the upcoming chapters as due to the nonlinear instability.

Moreover, all of the simulations other than the $n = 0$ suppressed simulation have qualitatively and semi-quantitatively similar statistical properties. I note that on a quantitative level, the Dirichlet and Neumann simulations have fluctuation levels about 1.5 times less than the Periodic and Sheath simulations. I don't fully understand the reason for this, but note that the axial wavenumber spectra in Fig. 5.7 f) are shallower for the Dirichlet and Neumann simulations. This certainly affects the energy injection and energy dissipation, as will be seen in the following chapters. Nevertheless, even though their fluctuation levels are too low, I don't claim that the Dirichlet and Neumann simulations are less consistent with the experiment than the Periodic and Sheath simulations. The reason is that I have a free parameter, namely the artificial diffusion coefficient, which affects the overall fluctuation level without significantly affecting the shapes of the spectra. I tuned this parameter to be 1.25×10^{-3} (see Chapter 4) to match

the fluctuation level of the Periodic simulation with experiment. Had I tuned this parameter with the Dirichlet or Neumann simulations in mind, it would seem that the Periodic and Sheath simulations had fluctuation levels too large. So, in fact, all four of these simulations are qualitatively consistent with the experiment, and they are also quantitatively consistent with the caveat that the quantitative match is caused by tuning a single free parameter. I don't provide any error analysis to quantify the agreement between simulation and experiment, but rather just use an eye test. The fact that several different statistical properties of several fields (see Fig. 5.6) agree between simulation and experiment lends evidence to my claim that the simulation model is relatively well validated.

One final statistical measurement that may be compared between simulation and experiment is the spatial correlation. Experimentally, this can be done by fixing one probe at a certain location and moving another probe around and measuring the correlation between the two I_{sat} signals. The second probe can scan the $r - \theta$ plane at an axial location close to the first probe. The results of the simulated spatial correlation compared to the experimental correlation are shown in Fig. 5.8. For the simulation, I show only the result from the Periodic simulation. The darkest red point, which has a correlation value of 1 marks the location of the stationary probe. The black line is the $1/e$ contour, where the distance from the stationary probe to this contour is the correlation length. The simulation correlation length of about 1 cm is about half of that of the experimental correlation length. Furthermore, neither have completely isotropic structure, and their slight divergences from isotropy are not that similar. However, there is no complex mode structure or long extended correlations in either one.
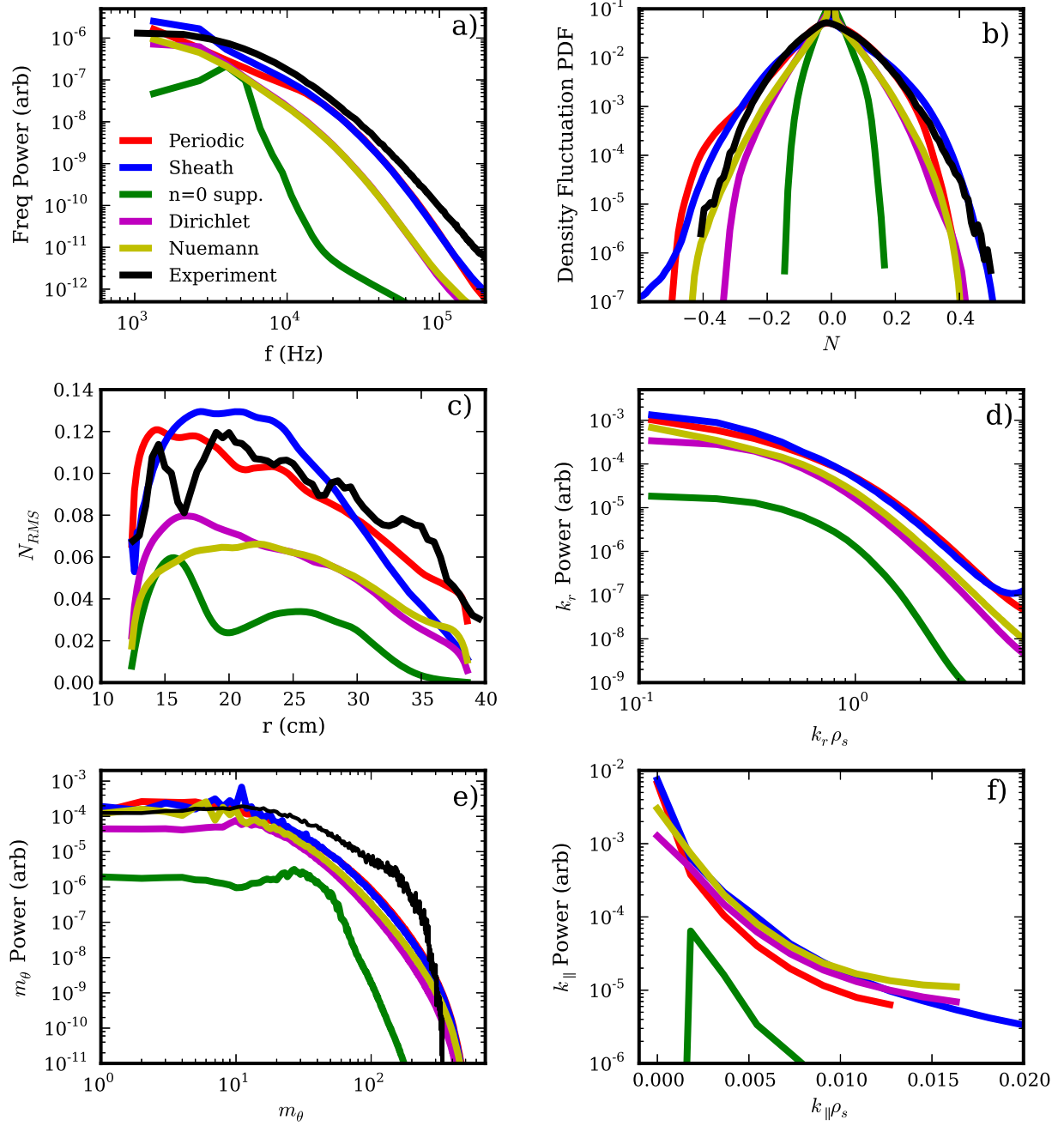
Figure 5.7: Density statistics
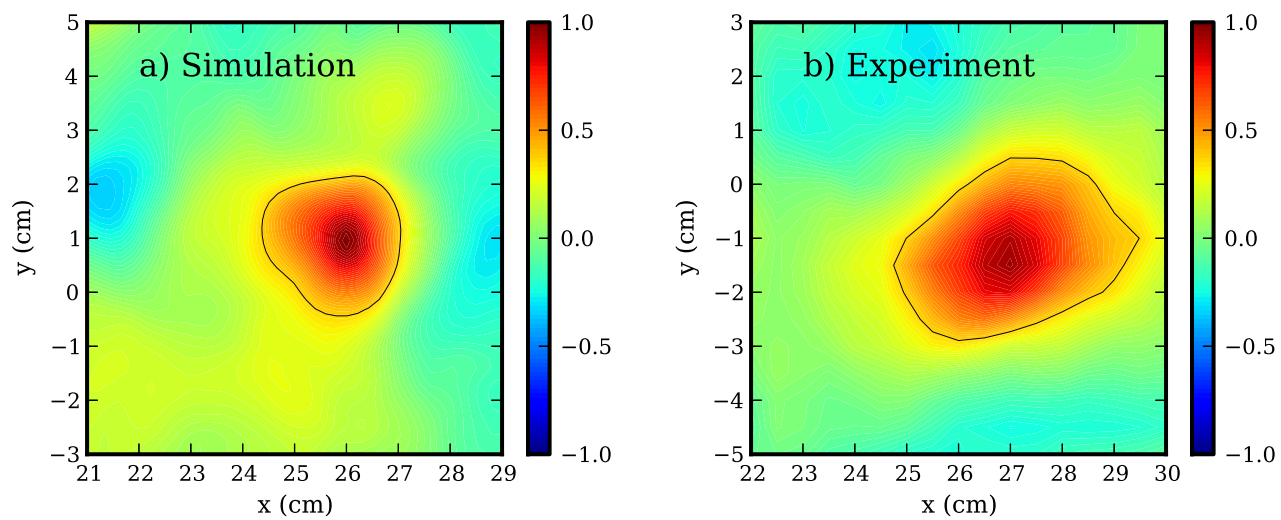
Figure 5.8: Spatial density correlations

CHAPTER 6

Energy Dynamics Formalism

In the last section of the previous chapter, I analyzed the experimental and simulated turbulence using simple and common statistical methods. Never did I assume any kind of model for the turbulence, nor did I take full advantage of the wealth of spatial information provided by the simulations. In the remaining chapters, I do use the simulated physics model along with the turbulent spatial structures to analyze the nature of the turbulence from an energy dynamics perspective. The energy dynamics provide direct information about energy injection into the turbulence from the equilibrium gradients, energy transfer among different fields and between different normal modes, and turbulent energy dissipation. This information allowed me to uncover the mysterious mechanism that drives the $n = 0$ fluctuations so strongly in the simulations (see Fig. 5.7 f)). The mechanism is a nonlinear instability. I will provide evidence for this in the next chapter, but in this chapter, I will derive the dynamical energy equations and explain what they mean.

6.1 Total Energy and Dynamics

First, I consider the total, volume-averaged energy and energy dynamics. The total volume-averaged energy of the fluctuations (in normalized units) is:

$$E = \frac{1}{2} \int_V \left[P_0 \left((N/N_0)^2 + \frac{3}{2}(T_e/T_{e0})^2 \right) + N_0 \left(\frac{m_e}{m_i} v_{\parallel e}^2 + (\nabla_\perp \phi)^2 \right) \right] dV, \quad (6.1)$$

where $P_0 = N_0 T_{e0}$ is the equilibrium pressure. The $\frac{1}{2}P_0(N/N_0)^2$ term is the potential energy due to density fluctuations, $\frac{3}{4}P_0(T_e/T_{e0})^2$ is the electron temperature fluctuation potential energy, $\frac{1}{2}N_0\frac{m_e}{m_i}v_{\|e}^2$ is the parallel electron kinetic energy, and $\frac{1}{2}N_0(\nabla_\perp\phi)^2$ is the $\mathbf{E}\times\mathbf{B}$ perpendicular kinetic energy. The energy contained in the electric field is smaller than the perpendicular kinetic energy by a factor of $(v_A/c)^2$ and is therefore neglected.

The dynamical energy evolution $\partial E/\partial t$ can be obtained using Eqs. 4.1- 4.4 in the following way. First, take Eq. 4.1 and multiply both sides by $\frac{T_{e0}}{N_0}N$ and integrate over the volume. The result is:

$$\frac{\partial E_N}{\partial t} = \left\langle -T_{e0}N\mathbf{v_E}\cdot\nabla\ln N_0 - T_{e0}N\nabla_\|v_{\|e} - \mu_N\frac{T_{e0}}{N_0}(\nabla_\perp N)^2 + \frac{T_{e0}}{N_0}NS_N \right\rangle, \quad (6.2)$$

where $E_N = \frac{1}{2}\left\langle P_0(N/N_0)^2\right\rangle$ with $\langle\rangle$ shorthand for the volume integral $\int_V dV$. Next, multiply Eq. 4.2 by $N_0\frac{m_e}{m_i}v_{\|e}$, Eq. 4.3 by $-\phi$, and Eq. 4.4 by $\frac{3}{2}\frac{N_0}{T_{e0}}T_e$ and volume integrate, giving:

$$\frac{\partial E_v}{\partial t} = \left\langle -T_{e0}v_{\|e}\nabla_\|N - 1.71N_0v_{\|e}\nabla_\|T_e + N_0v_{\|e}\nabla_\|\phi - \frac{m_e}{m_i}N_0\nu_e v_{\|e}^2 \right\rangle, (6.3)$$

$$\frac{\partial E_\phi}{\partial t} = \left\langle N_0\phi\nabla_\|v_{\|e} - \nu_{in}N_0(\nabla_\perp\phi)^2 - \mu_\phi\phi\nabla_\perp^2\varpi \right\rangle, \quad (6.4)$$

$$\frac{\partial E_T}{\partial t} = \left\langle -\frac{3}{2}N_0T_e\mathbf{v_E}\cdot\nabla\ln T_{e0} - 1.71N_0T_e\nabla_\|v_{\|e} - \kappa_{\|e}/T_{e0}(\nabla_\|T_e)^2 \right\rangle$$
$$+ \left\langle -\frac{3m_e}{m_i}\frac{N_0}{T_{e0}}\nu_e T_e^2 - \frac{3}{2}\mu_T\frac{N_0}{T_{e0}}(\nabla_\perp T_e)^2 + \frac{3}{2}\frac{N_0}{T_{e0}}T_eS_T \right\rangle, \quad (6.5)$$

where $E_v = \frac{1}{2}\left\langle N_0\frac{m_e}{m_i}v_{\|e}^2\right\rangle$, $E_\phi = \frac{1}{2}\left\langle N_0(\nabla_\perp\phi)^2\right\rangle$, and $E_T = \frac{3}{4}\left\langle P_0(T_e/T_{e0})^2\right\rangle$.

Note that there are a few simplifications made in these equations. One simplification is that the term $\left\langle\mu_N\frac{T_{e0}}{N_0}N\nabla_\perp^2 N\right\rangle$ is written approximately as $-\left\langle\mu_N\frac{T_{e0}}{N_0}(\nabla_\perp N)^2\right\rangle$ in Eq. 6.2. The fact that $\frac{T_{e0}}{N_0}\approx 1$ makes this approximation acceptable. In fact, I don't use this approximation when calculating such quantities from the simulations, but I write it here as it illuminates the fact that this energy term

is negative. I use the same approximation with the $-\left\langle \frac{3}{2}\mu_T \frac{N_0}{T_{e0}}(\nabla_\perp T)^2 \right\rangle$ and $-\left\langle \kappa_{\|e}/T_{e0}(\nabla_\| T_e)^2 \right\rangle$ terms, although the latter contains the fraction $\kappa_{\|e}/T_{e0}$, which is not necessarily close to being constant.

Moreover, notice that none of the advective nonlinear terms are present in these energy dynamics equations. The reason is that $\langle f\{g,f\} \rangle = 0$, which holds as long as all of the boundaries are periodic, have $f = 0$ boundaries, or have $\nabla g \cdot d\vec{S} = 0$ boundaries. Now only Eq. 6.4 actually has this $\langle f\{g,f\} \rangle$ form for its nonlinearity because all of the other energy equations contain equilibrium profile quantities in the volume average (e.g. $\left\langle \frac{T_{e0}}{N_0}N\{\phi,N\} \right\rangle$ in Eq. 6.2). Nevertheless, the equilibrium profile quantities come as $\frac{T_{e0}}{N_0} \approx 1$ for Eq. 6.2 and $\frac{N_0}{T_{e0}} \approx 1$ for Eq. 6.5, while there is a factor of the electron to ion mass ratio multiplied by the nonlinearity in Eq. 6.3. This means that all of the nonlinearities approximately vanish in the energy equations. Furthermore, I have confirmed this by direct calculation of these terms. This is why I do not include the nonlinearities in Eqs. 6.2- 6.5.

I note that I could have used a different expression for the energy in order to absolutely conserve the nonlinearities. For instance, I could have set $E_N = \frac{1}{2}\langle N^2 \rangle$, neglecting the factor $\frac{T_{e0}}{N_0}$. In fact, I did this in the Friedman et al. paper [FCU12]. However, this expression would not be the physical energy, although it would have the convenient property of conserving the nonlinearities. Energy, after all, is a useful concept because it's a conserved quantity. Nevertheless, I have chosen to use the physical energy in this work as well as in another paper [FCU13] because the physical energy conserves the adiabatic response. I will show this below. Furthermore, the physical energy very nearly conserves the nonlinearities, so it's not a big problem to use the physical energy. The calculated error of neglecting the nonlinearities in the energy dynamics equations is only about 1%. Now, one may wonder why the physical energy doesn't absolutely conserve the advective nonlinearities. The answer lies in the partial linearization of the simulation equa-

tions. The linearization neglects many nonlinear contributions that are needed for global energy conservation. Nevertheless, I find that the spectral energy dynamics analysis in Sec. 6.2 is simpler when I neglect most of the nonlinearities.

Now Eqs. 6.2- 6.5 are still not increadibly revealing because they contain nearly as many terms as the original simulated equations. However, I can break each of these equations down in the following way:

$$\frac{\partial E_j}{\partial t} = Q_j + C_j + D_j. \tag{6.6}$$

The subscript j represents the individual field: (N, v, ϕ, T). Q_j represents energy injection from an equilibrium gradient. For example, Q_N represents the energy injected into E_N (the density fluctuation potential energy) taken from the free energy of the equilibrium density gradient ($\nabla_r N_0$). These terms are:

$$Q_N = \langle -T_{e0} N \mathbf{v_E} \cdot \nabla \ln N_0 \rangle, \tag{6.7}$$

$$Q_v = 0, \tag{6.8}$$

$$Q_\phi = 0, \tag{6.9}$$

$$Q_T = \left\langle -\frac{3}{2} N_0 T_e \mathbf{v_E} \cdot \nabla \ln T_{e0} \right\rangle. \tag{6.10}$$

Only the density and temperature fluctuations receive energy from the equilibrium density and temperature gradients, respectively. They do so by radial $\mathbf{E} \times \mathbf{B}$ advection, moving fluid or heat across the gradient where it can enhance or diminish the density and temperature fluctuations. I call the Q_j terms energy injection terms, but they can in fact dissipate fluctuation energy if the phase between the density (or temperature) and potential are stabilizing.

Next, the C_j terms represent transfer channels. They are:

$$C_N = \langle -T_{e0} N \nabla_\parallel v_{\parallel e} \rangle, \tag{6.11}$$

$$C_v = \left\langle -T_{e0}v_{\|e}\nabla_\| N - 1.71N_0v_{\|e}\nabla_\| T_e + N_0v_{\|e}\nabla_\| \phi \right\rangle, \tag{6.12}$$

$$C_\phi = \left\langle N_0\phi\nabla_\| v_{\|e} \right\rangle, \tag{6.13}$$

$$C_T = \left\langle -1.71N_0T_e\nabla_\| v_{\|e} \right\rangle. \tag{6.14}$$

Notice that $C_N + C_\phi + C_T = -C_v$ if the axial boundaries are periodic or zero value. Alternatively, $\sum_j C_j = 0$. So no energy is gained or lost in total. Energy does, however, transfer between the different fields: $N, T_e, \phi \leftrightarrow v_{\|e}$. All energy transfers through the parallel electron velocity. The density, temperature, and potential fluctuations all feed or draw energy from the parallel electron velocity. The equations allow no state variable energy transfer. For instance, the density and potential fluctuations cannot transfer energy between each other directly. Recall that this is the mechanism of the adiabatic response (see Sec. 5.1). I commented on the conservation of energy of the adiabatic response above when discussing the use of the physical energy, and this is what I meant. Note that the "energy-like" expression used in one of our papers [FCU12] that absolutely conserved the advective nonlinearities did not come close to conserving the adiabatic response energy. That's why in this work and in another paper [FCU13], I chose to use the physical energy.

I inject two minor points concerning the boundary conditions. The first is that the Neumann and sheath simulations don't exactly conserve the adiabatic response because of non-vanishing contributions from the boundaries. Second, the sheath boundary conditions allow energy transfer between the temperature and potential fluctuations without the adiabatic response. That transfer mechanism isn't represented in the C_j expressions. I will calculate it in Chapter 8.

Finally, the D_j terms represent dissipative energy loss from the fluctuations. They are:

$$D_N = \left\langle -\mu_N\frac{T_{e0}}{N_0}(\nabla_\perp N)^2 + \frac{T_{e0}}{N_0}NS_N \right\rangle, \tag{6.15}$$

53

$$D_v = \left\langle -\frac{m_e}{m_i} N_0 \nu_e v_{\parallel e}^2 \right\rangle, \tag{6.16}$$

$$D_\phi = \left\langle -\nu_{in} N_0 (\nabla_\perp \phi)^2 - \mu_\phi \phi \nabla_\perp^2 \varpi \right\rangle, \tag{6.17}$$

$$D_T = \left\langle -\kappa_{\parallel e}/T_{e0} (\nabla_\parallel T_e)^2 - \frac{3m_e}{m_i} \frac{N_0}{T_{e0}} \nu_e T_e^2 \right\rangle$$

$$+ \left\langle -\frac{3}{2} \mu_T \frac{N_0}{T_{e0}} (\nabla_\perp T_e)^2 + \frac{3}{2} \frac{N_0}{T_{e0}} T_e S_T \right\rangle. \tag{6.18}$$

Most of these terms are clearly negative. However, the source terms do not have a clear sign and the $\langle -\mu_\phi \phi \nabla_\perp^2 \varpi \rangle$ viscous term in Eq. 6.17 doesn't have a clear sign either. Recall, though, that the sources essentially remove the flux-surface averaged component of the density and temperature fluctuations, indicating that they remove the energy associated with these fluctuation components. Taking $S_N \approx -\langle N \rangle_{fs}$ from Eqs. 4.5 and 4.6, then the source contribution to D_N is $-\left\langle \frac{T_{e0}}{N_0} \langle N \rangle_{fs}^2 \right\rangle$, which is negative. The viscous term in Eq. 6.17 is less obviously negative, however, letting $\nabla_\perp \to -k_\perp^2$ makes the viscous term approximately $-\langle \mu_\phi N_0 k_\perp^4 \phi^2 \rangle$. So it's reasonable to conclude that all contributions in the D_j expressions are absolutely negative. My direct calculations have confirmed this.

6.2   Spectral Energy Dynamics

While the total energy dynamics can reveal some important information such as the amount of energy entering the density fluctuations vs. the temperature fluctuations, the direction of energy flow through the adiabatic response, and how much energy is dissipated by the various mechanisms, the total dynamics cannot show the mechanism of the nonlinear instability. In fact, the total energy dynamics are rather useless in revealing any nonlinear physics. Spectral or mode-decomposed energy dynamics, on the other hand, provide much more information regarding mode-specific processes like cascades and complex nonlinear processes.

When deriving mode-decomposed energy dynamics, one first has to choose a set of basis functions. As long as the functions form an independent complete

basis, they are acceptable. Fourier modes are a natural basis to use for any coordinate with periodic boundaries. Fourier modes are also orthogonal to one another, making them ideal. Linear eigenmodes provide another good choice for a basis; however, they can be non-orthogonal in some systems, making them somewhat unweildy. I began this study using a linear eigenmode decomposition, but I eventually gave up that path because the linear eigenmodes of this system are non-orthogonal. The results were complicated and didn't show anything more interesting than a simpler Fourier decomposition would show. Hatch et al. dealt with this non-orthogonality problem with two distinct methods [HTJ11]. The first was to use a Gram-Schmidt orthogonalization procedure starting with the most unstable linear eigenmode to make the modes orthogonal. The resulting modes other than the most unstable linear eigenmode, however, were no longer the linear eigenmodes. The second method was to use a proper orthogonal decomposition (POD, which is essentially a kind of singular value decomposition) to create orthogonal modes that best captured the dominant turbulent structures. Both of these methods are very interesting and quite useful for some systems, however, they are probably most useful for systems with strong linear instabilities where most of the energy of the turbulence is contained in the fastest growing linear eigenmode or a dominant POD mode. That is not the case for the LAPD turbulence.

I found that the most useful basis to take is a partial Fourier basis. Namely, I simply use a Fourier decomposition in the azimuthal and axial directions. For example, I decompose the density in the following way:

$$N(r, \theta, z, t) = \sum_{\vec{k}} n_{\vec{k}}(r, t) e^{i(m\theta + k_z z)}. \tag{6.19}$$

Here, $k_z = \frac{2\pi n}{L_{\parallel} \rho_s}$, where n is the axial mode number and m is the azimuthal mode number, and the $\vec{k}$ symbol is short for (m, n). The sum over $\vec{k}$ is in fact

a double sum over m and n. Furthermore, positive and negative m and n are included in the sums to ensure reality of N since $n_{-\vec{k}} = n_{\vec{k}}^*$. Similar decompositions are used for $v_{\parallel e}, \phi$, and T_e. Note that the radial part of the basis function $n_{\vec{k}}(r, t)$ is time-dependent and shouldn't really be called a basis function at all because of this. I cannot say anything about nonlinear processes involving different radial modes since I haven't decomposed the radial structures into a time-independent basis. Essentially, I have limited the amount of information I can gain from this decomposition. I have intentionally done this to focus on a few particular results, which would be more difficult to see if I used an additional radial decomposition.

To derive the spectral energy equations, I first substitute the Fourier decompositions into Eqs. 4.1- 4.4. Using the density evolution equation as an example, I get:

$$\sum_{\vec{k}} \frac{\partial n_{\vec{k}}}{\partial t} e^{i(m\theta + k_z z)} =$$
$$\sum_{\vec{k}} \left[-\frac{im}{r} \partial_r N_0 \phi_{\vec{k}} - ik_z N_0 v_{\vec{k}} + \mu_N (\partial_r^2 n_{\vec{k}} + \frac{1}{r} \partial_r n_{\vec{k}} - \frac{m^2}{r^2} n_{\vec{k}}) \right] e^{i(m\theta + k_z z)}$$
$$+ \frac{1}{r} \sum_{\vec{k}, \vec{k}'} (imn_{\vec{k}} \partial_r \phi_{\vec{k}'} - im' \partial_r n_{\vec{k}} \phi_{\vec{k}'}) e^{i(m+m')\theta + i(k_z + k_z')z} + S_N. \qquad (6.20)$$

Note the double sum for the nonlinearity. Continuing on with just the density equation for now, I proceed to get the energy equation by multiplying through by $\frac{T_{e0}}{N_0} n_{\vec{k}''}^* e^{-im''\theta - ik_z''z}$ and integrating over space. The result is (with primes permuted):

$$\frac{1}{2} \left\langle \frac{T_{e0}}{N_0} \frac{\partial |n_{\vec{k}}|^2}{\partial t} \right\rangle =$$
$$\left\langle -\frac{T_{e0}}{N_0} \frac{im}{r} \partial_r N_0 \phi_{\vec{k}} n_{\vec{k}}^* - ik_z T_{e0} v_{\vec{k}} n_{\vec{k}}^* + \frac{T_{e0}}{N_0} \mu_N (\partial_r^2 n_{\vec{k}} + \frac{1}{r} \partial_r n_{\vec{k}} - \frac{m^2}{r^2} n_{\vec{k}}) n_{\vec{k}}^* \right\rangle$$

56

$$+ \left\langle \frac{T_{e0}}{rN_0} \sum_{\vec{k}'} \left(im' n_{\vec{k}'} \partial_r \phi_{\vec{k}-\vec{k}'} n_{\vec{k}}^* - i(m-m') \partial_r n_{\vec{k}'} \phi_{\vec{k}-\vec{k}'} n_{\vec{k}}^* \right) \right\rangle$$

$$+ \left\langle \frac{T_{e0}}{N_0} S_N n_{\vec{k}=0}^* \right\rangle, \tag{6.21}$$

where the brackets now represent the reality operator and the radial integral $Re\left\{ \int r dr \right\}$ because I have performed the azimuthal and axial integrations and taken the real part of the equation. Breaking this up into specific parts:

$$\frac{\partial E_N(\vec{k})}{\partial t} = Q_N(\vec{k}) + C_N(\vec{k}) + D_N(\vec{k}) + \sum_{\vec{k}'} T_N(\vec{k},\vec{k}') \tag{6.22}$$

with

$$E_N(\vec{k}) = \frac{1}{2} \left\langle \frac{T_{e0}}{N_0} |n_{\vec{k}}|^2 \right\rangle \tag{6.23}$$

$$Q_N(\vec{k}) = \left\langle -\frac{im}{r} \frac{T_{e0}}{N_0} \partial_r N_0 \phi_{\vec{k}} n_{\vec{k}}^* \right\rangle \tag{6.24}$$

$$C_N(\vec{k}) = \left\langle -ik_z T_{e0} v_{\vec{k}} n_{\vec{k}}^* \right\rangle \tag{6.25}$$

$$D_N(\vec{k}) = \left\langle \frac{T_{e0}}{N_0} \mu_N (\partial_r^2 n_{\vec{k}} + \frac{1}{r} \partial_r n_{\vec{k}} - \frac{m^2}{r^2} n_{\vec{k}}) n_{\vec{k}}^* + \frac{T_{e0}}{N_0} S_N n_{\vec{k}=0}^* \right\rangle \tag{6.26}$$

$$T_N(\vec{k},\vec{k}') = \left\langle \frac{T_{e0}}{rN_0} \left(im' n_{\vec{k}'} \partial_r \phi_{\vec{k}-\vec{k}'} n_{\vec{k}}^* - i(m-m') \partial_r n_{\vec{k}'} \phi_{\vec{k}-\vec{k}'} n_{\vec{k}}^* \right) \right\rangle \tag{6.27}$$

The new piece not in the total energy dynamics in Sec. 6.1, $T_N(\vec{k},\vec{k}')$, comes from the advective nonlinearity. It couples different Fourier modes, meaning that it transfers energy between different $\vec{k}$ waves. It is not conserved for individual $\vec{k}$ modes, but is conserved on the aggregate, meaning $\sum_{\vec{k},\vec{k}'} T_N(\vec{k},\vec{k}') \simeq 0$. Notice also that $Q_N(\vec{k})$ can be finite for $n = 0$, but $C_N(\vec{k})$ is zero for $n = 0$. In other words, flute modes may take energy from the equilibrium density gradient, but they cannot access the adiabatic response. This precludes linear drift wave flute modes. But it does not preclude nonlinear drift wave flute modes because they can transfer their energy to non-flute structures in order to access the adiabatic response.

For completeness, I write the rest of the spectral energy dynamics pieces here. The perpendicular kinetic energy dynamics pieces are:

$$E_\phi(\vec{k}) = \frac{1}{2}\left\langle N_0\left|\frac{\partial \phi_{\vec{k}}}{\partial r}\right|^2 + N_0\frac{m^2}{r^2}|\phi_{\vec{k}}|^2\right\rangle \tag{6.28}$$

$$Q_\phi(\vec{k}) = 0 \tag{6.29}$$

$$C_\phi(\vec{k}) = \left\langle ik_z N_0 v_{\vec{k}}\phi_{\vec{k}}^*\right\rangle \tag{6.30}$$

$$D_\phi(\vec{k}) = \left\langle -\mu_\phi(\partial_r^2\varpi_{\vec{k}} + \frac{1}{r}\partial_r\varpi_{\vec{k}} - \frac{m^2}{r^2}\varpi_{\vec{k}})\phi_{\vec{k}}^* - \nu_{in}E_\phi(\vec{k})\right\rangle \tag{6.31}$$

$$T_\phi(\vec{k},\vec{k}') = \left\langle -\frac{1}{r}\left(im'\varpi_{\vec{k}'}\partial_r\phi_{\vec{k}-\vec{k}'}\phi_{\vec{k}}^* - i(m-m')\partial_r\varpi_{\vec{k}'}\phi_{\vec{k}-\vec{k}'}\phi_{\vec{k}}^*\right)\right\rangle \tag{6.32}$$

and for the electron temperature potential energy:

$$E_T(\vec{k}) = \frac{3}{4}\left\langle \frac{N_0}{T_{e0}}|t_{\vec{k}}|^2\right\rangle \tag{6.33}$$

$$Q_T(\vec{k}) = \left\langle -\frac{3}{2}\frac{N_0}{T_{e0}}\frac{im}{r}\partial_r T_{e0}\phi_{\vec{k}}t_{\vec{k}}^*\right\rangle \tag{6.34}$$

$$C_T(\vec{k}) = \left\langle -1.71ik_z N_0 v_{\vec{k}}t_{\vec{k}}^*\right\rangle \tag{6.35}$$

$$D_T(\vec{k}) = \left\langle -\frac{\kappa_{\|e}}{T_{e0}}k_z^2|t_{\vec{k}}|^2 - \frac{3m_e}{m_i}\frac{N_0}{T_{e0}}\nu_e|t_{\vec{k}}|^2\right\rangle$$
$$+ \left\langle \frac{3}{2}\frac{N_0}{T_{e0}}\mu_T(\partial_r^2 t_{\vec{k}} + \frac{1}{r}\partial_r t_{\vec{k}} - \frac{m^2}{r^2}t_{\vec{k}})t_{\vec{k}}^* + \frac{3}{2}\frac{N_0}{T_{e0}}S_T t_{\vec{k}=0}^*\right\rangle \tag{6.36}$$

$$T_T(\vec{k},\vec{k}') = \left\langle \frac{3}{2r}\frac{N_0}{T_{e0}}\left(im't_{\vec{k}'}\partial_r\phi_{\vec{k}-\vec{k}'}t_{\vec{k}}^* - i(m-m')\partial_r t_{\vec{k}'}\phi_{\vec{k}-\vec{k}'}t_{\vec{k}}^*\right)\right\rangle \tag{6.37}$$

and for the parallel kinetic energy:

$$E_v(\vec{k}) = \frac{1}{2}\frac{m_e}{m_i}\left\langle N_0|v_{\vec{k}}|^2\right\rangle \tag{6.38}$$

$$Q_v(\vec{k}) = 0 \tag{6.39}$$

$$C_v(\vec{k}) = \left\langle -ik_z N_0 n_{\vec{k}}v_{\vec{k}}^* + ik_z N_0\phi_{\vec{k}}v_{\vec{k}}^* - 1.71ik_z T_{e0}t_{\vec{k}}v_{\vec{k}}^*\right\rangle \tag{6.40}$$

$$D_v(\vec{k}) = \left\langle -\nu_e\frac{m_e}{m_i}N_0|v_{\vec{k}}|^2\right\rangle \tag{6.41}$$

$$T_v(\vec{k},\vec{k}') = \left\langle \frac{m_e}{m_i}\frac{N_0}{r}\left(im'v_{\vec{k}'}\partial_r\phi_{\vec{k}-\vec{k}'}v_{\vec{k}}^* - i(m-m')\partial_r v_{\vec{k}'}\phi_{\vec{k}-\vec{k}'}v_{\vec{k}}^*\right)\right\rangle . \tag{6.42}$$

58

CHAPTER 7

Nonlinear Instability for the Periodic Simulation

In this chapter, I use the energy dynamics machinery developed in the last chapter to show where in wavenumber space and to which fields energy is deposited, how it's transferred, and where it's dissipated. I show that the linear instability plasma paradigm doesn't hold for the LAPD simulations, but rather, a complex nonlinear instability process dominates the energy dynamics. Furthermore, in this chapter, I consider only the simulations with periodic boundary conditions: the Periodic simulation and the $n = 0$ suppressed simulation. I analyze the remaining simulations (Dirichlet, Neumann, and Sheath) in the next chapter.

7.1 The Energy Spectra

Although I have already discussed the relative importance of the $n = 0$ fluctuation flute structures and shown evidence for this in Figs. 5.3, 5.4, and 5.7, I now use the energy expressions in Eqs. 6.23, 6.28, 6.33, and 6.38 to show a detailed look at the energy wavenumber spectra. The spectra for the four fields in (m, n) space are shown in Fig. 7.1. As expected from Figs. 5.3, 5.4, and 5.7, most of the density energy $E_N(\vec{k})$ is located at $n = 0$ (and $1 < m < 10$). This wavenumber location is much different from my expectation which was that of the fastest growing linear eigenmode, which is at $(n = 1, m = 60)$. Additionally, $E_T(\vec{k})$ and $E_\phi(\vec{k})$ have similar-looking spectra as $E_N(\vec{k})$, though the actual magnitudes of the energy are quite different for the three fields. Finally, $E_v(\vec{k})$ has a remarkably different energy spectrum than the other fields. Most of the energy is contained at $n \geq 1$
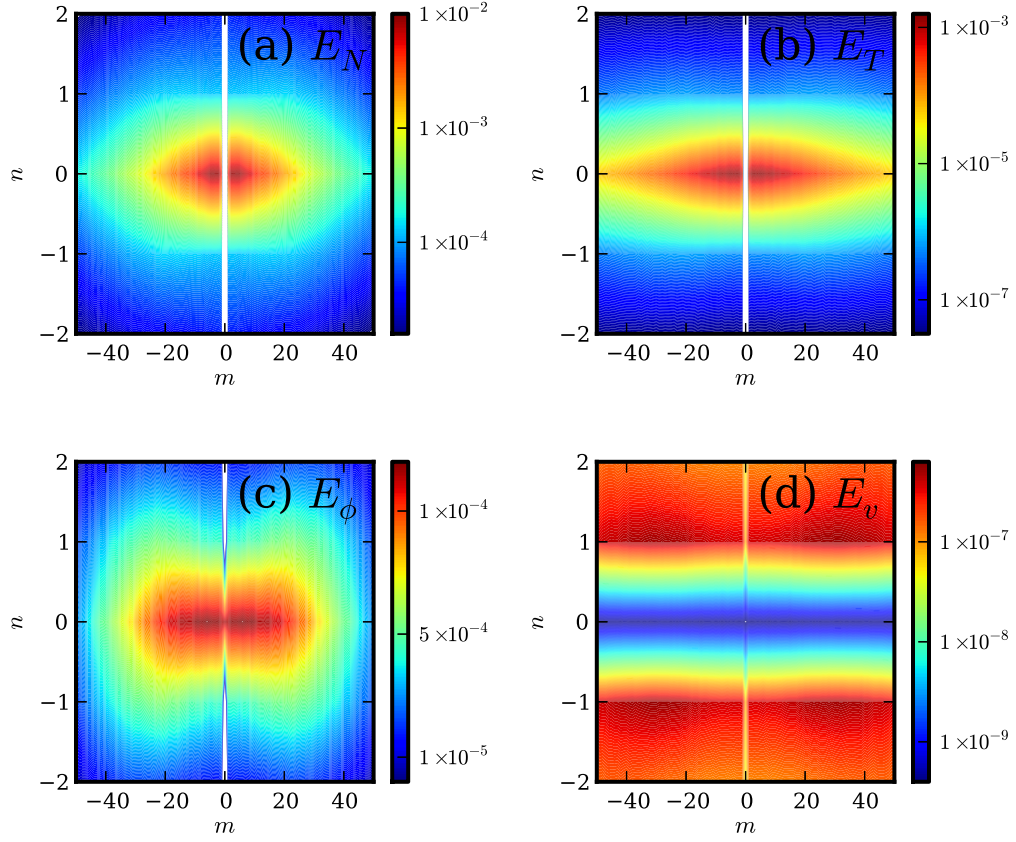
Figure 7.1: Energy k-Spectra

and $m \sim 30$, which is somewhat similar to the linear eigenmode growth rate spectrum, though m is lower.

Although these results are rather unexpected given the hypothesis that the most unstable linear eigenmode should pump energy into the turbulent system, one could still build upon this hypothesis to explain the nature of the spectra. In fact, in Ref. [UPC11], my collaborators and I posited and tested this hypothesis. Our specific hypothesis was that the most unstable linear eigenmode pumped energy into the system at its characteristic wavenumber and then proceeded to cascade energy forward and backward into other waves. The inverse cascade into $n = 0$ would be particularly strong to account for all of the energy in the $n = 0$

Fourier components.

Our test of this inverse cascade revolved around the use of a particular bi-coherence three wave interaction, namely that between three density fluctuation Fourier modes of $(n, m) = (1, 25), (-1, -24)$ and $(0, 1)$. Note that in that study, we used a different set of profiles and parameters for the simulation than the one I use in this report, and the dominant azimuthal mode numbers in that study were smaller than those in this report. In any case, in Ref. [UPC11], we found a strong bicoherence amplitude for this three-wave interaction and assumed that this meant that the waves with $(n, m) = (1, 25)$ and $(-1, -24)$ coupled to transfer their energy to waves with $(0, 1)$. This fit within the standard linear instability paradigm because linear eigenmodes with $(n, m) \sim (\pm 1, \pm 25)$ were the most unstable for that system. Unfortunately, bicoherence is only a vague proxy for three-wave energy interaction, and it doesn't indicate a direction of energy transfer. As I later worked on energy dynamics calculations, I discovered, to my surprise, that we had the direction of energy transfer backwards! Our assumption regarding the direction of energy transfer was wrong. The paradigmatic plasma turbulence view led us astray.

7.2   Energy Dynamics Results

7.2.1   Dynamics Details

The full energy dynamics analysis using the machinery of Chapter 6 removes any ambiguity regarding the locations and magnitudes of energy injection into the fluctuations and direction of energy transfer between different Fourier modes. In fact, the full dynamics contains so much information that it can be difficult to digest it all. I therefore try to focus on the most important parts, especially those that are crucial to the nonlinear instability. First, in Fig. 7.2, I show values for some of the Q_j, C_j, and D_j terms in the energy dynamics equations for $n = 0, \pm 1$
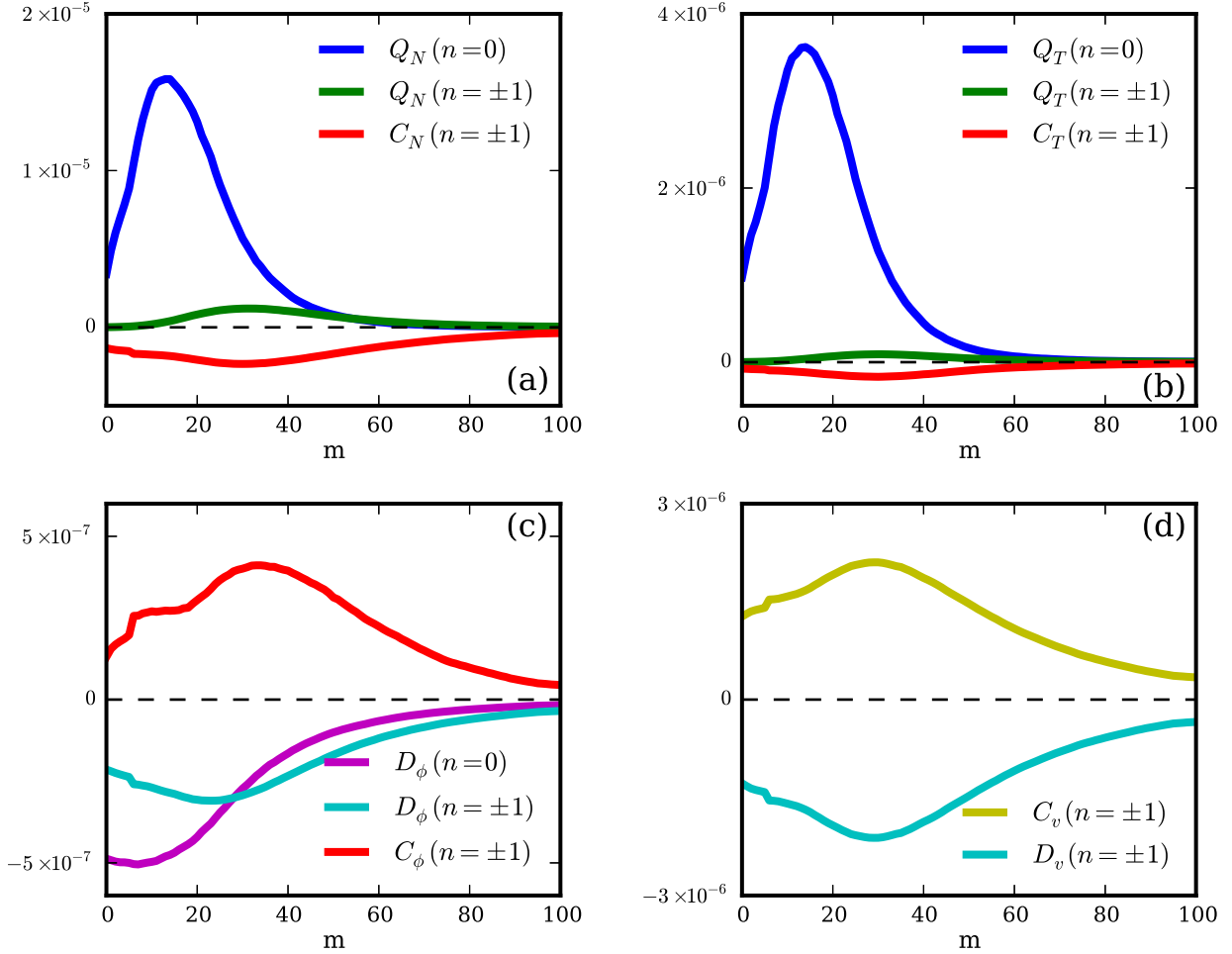
Figure 7.2: Periodic simulation energy dynamics

and $0 \leq m \leq 100$, neglecting all dynamics with $|n| \geq 2$, which have relatively small values and are mostly insignificant. The dynamics curves are all averaged over a time period during the turbulent stage of the simulation where the dynamics processes have all reached a quasi-steady state. The label $n = \pm 1$ represents the addition of terms with $n = 1$ and $n = -1$. Fig. 7.2 a) reveals the density potential energy injection (Q_N) and the adiabatic response transfer (C_N). I don't show the dissipation (D_N) in this figure, which is why the curves don't seem to add

up to zero as they would if all dynamics were shown. Nevertheless, this figure immediately reveals that the majority of the energy is injected straight into the $n = 0$ fluctuations from the equilibrium density gradient rather than into the $n = \pm 1$ fluctuations! Looking at Eq. 6.24 again, and I reiterate, $Q_N(\vec{k})$ does not depend on n, so it is perfectly acceptable to inject energy straight into $n = 0$ fluctuations. However, $C_N(\vec{k})$ is proportional to n (Eq. 6.25), so energy can only travel through the adiabatic response path in finite n structures. This is why the unstable linear eigenmodes have finite n – because eigenmodes with $n = 0$ cannot access the adiabatic response and thus have no field coupling. But with nonlinearities involved, there is nothing to prevent energy extraction at $n = 0$. Likewise, Fig. 7.2 b) reveals the same kind of story for the temperature potential energy, although the magnitudes are quite low compared to the density ones, indicating that the temperature fluctuations are relatively insignificant as a player in the total energy dynamics.

Fig. 7.2 c) shows the perpendicular kinetic energy dynamics. Recall $Q_\phi = 0$, so there is no direct energy injection; rather, energy enters ϕ fluctuations via the adiabatic response (C_ϕ). Even though no energy enters ϕ at $n = 0$, flute-like dissipation $D_\phi(n = 0)$ is significant, forshadowing the need for three-wave energy transfer into $n = 0$ ϕ fluctuations. Additionally, although I don't show $|n| \geq 2$ dynamics, they are somewhat important for C_ϕ and D_ϕ, accounting for the obviously unbalanced dynamics in this figure. Lastly, Fig. 7.2 d) reveals the parallel kinetic energy dynamics, which simply includes the adiabatic transfer (C_v) and electron-ion frictional dissipation (D_v). Recall that $C_N + C_\phi + C_T = -C_v$ for each $\vec{k}$. In other words, looking at the C_j terms altogether, one can see that energy is drawn from the density and potential fluctuations into the $v_{\|e}$ fluctuations and then moves onto the electrostatic potential ϕ fluctuations. That is only clear when looking at all of the C_j taken together.

Fig. 7.2 only shows the dynamical pieces due to the linear terms of Eqs. 4.1-
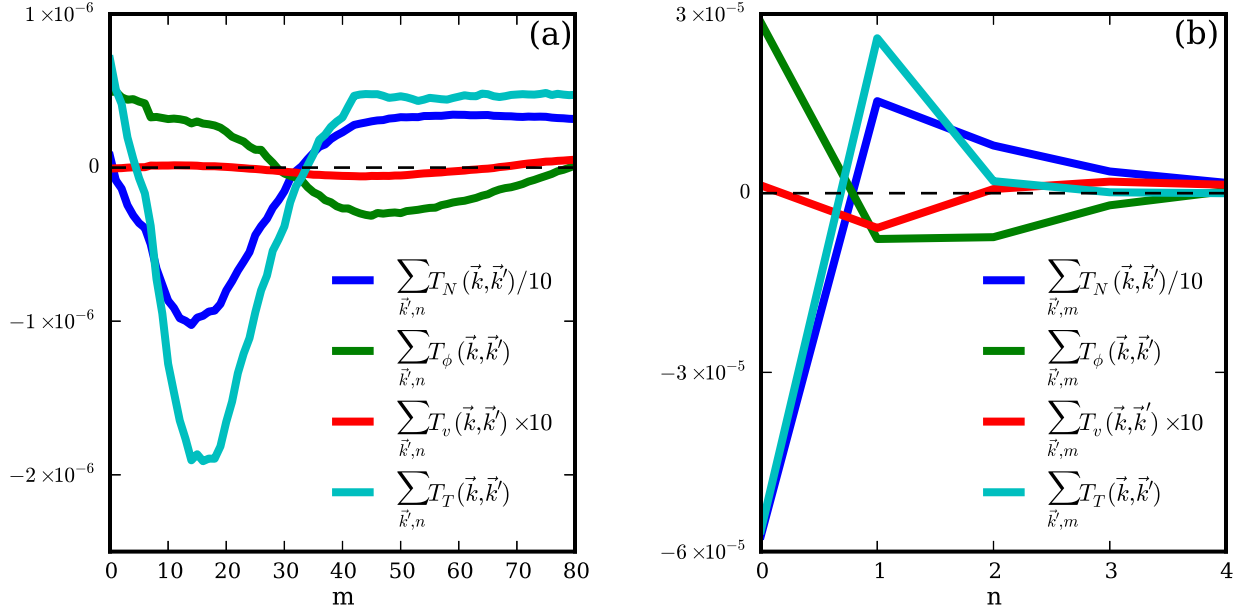
Figure 7.3: Periodic simulation three-wave transfer dynamics

4.4, and they therefore don't show the nonlinear transfer between different $\vec{k}$. The advective nonlinearities provide this transfer (the $T_j(\vec{k}, \vec{k}')$ terms), and they are essentially conservative, meaning they provide no net injection or dissipation with respect to the fluctuations. Now the $T_j(\vec{k}, \vec{k}')$ terms are each four dimensional, making them difficult to show. I choose to sum over some of the dimensions to show some of their aggregate properties. In Fig. 7.3 a), I sum over $\vec{k}'$ and n leaving them as only functions of m. Also note that I have divided $T_N(\vec{k}, \vec{k}')$ by 10 and multiplied $T_v(\vec{k}, \vec{k}')$ by 10 so that all of the T_j can be shown on one plot. Notice where T_N and T_T are positive and where they are negative. Negative values at a particular m indicate that the fluctuations with azimuthal wavenumber m are giving up net energy, while positive values correspond to fluctuations that are taking up net energy at that m. T_N and T_T transfer, on the aggregate, energy in the range $5 < m < 30$ to energy at all other values of m. This is not at all surprising because Q_N and Q_T are largest for $5 < m < 30$. This means that energy is

injected from the equilibrium gradients at $5 < m < 30$ and then three-wave transferred into other azimuthal wave numbers in both forward and inverse cascades (mostly forward). Actually the summation I use hides the information regarding the locality of wavenumber transfer, so it's indeterminate from this figure whether the transfer process is by cascading or non-local transfer. I defer this detail to future work. On the other hand, T_ϕ and T_v have the opposite character of T_N and T_T, meaning that the transfer dynamics are the other way around. This is typical in similar systems, such as Hasegawa-Wakatani systems [HW83, CBS95] in which the density potential energy exhibits a forward cascade, while the perpendicular kinetic energy exhibits an inverse cascade. It was also obvious that this had to happen given the azimuthal assymetry between C_ϕ and D_ϕ (see Fig. 7.2 c)).

More importantly, however, Fig. 7.3 b) shows the axial wavenumber transfers. Again T_N and T_T are similar. Both show energy transfer from $n = 0$ to $n \neq 0$. This is truly important! It is the most direct evidence for the nonlinear instability. Our paradigmatic hypothesis in Ref. [UPC11] posited the opposite transfer direction. The most unstable linear eigenmodes have $n = \pm 1$ and all eigenmodes with $n = 0$ are stable, yet Fig. 7.3 b) shows that the dominant energy transfer is from $n = 0$ to $n \neq 0$, at least for N and T_e. Again, T_ϕ and T_v have the opposite character of T_N and T_T, as really they must, since ϕ and $v_{\parallel e}$ gain their energy through the adiabatic response.

It's still difficult to see the energy flow paths from Figs. 7.2 and 7.3 alone. So I have put the results in a flow diagram – Fig. 7.4. In order to do this, I've summed all quantities over m and n (including $|n| \geq 2$), except that I have left $n = 0$ components out of the sums and shown them separately. For instance, $Q_N(0)$ represents the density fluctuation energy injection at $n = 0$, while $Q_N(!0)$ represents the density fluctuation energy injection for all $n \neq 0$ summed together. Furthermore, the symbol $N(0)$ represents $\sum_m E_N(m, n = 0)$, $N(!0)$ represents $\sum_{m,n\neq 0} E_N(\vec{k})$, etc. Note that every term is summed over m.
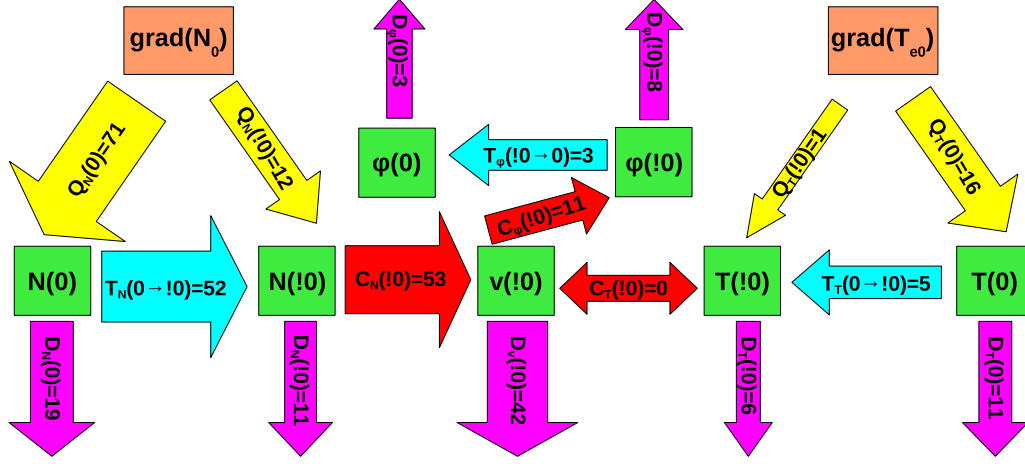
Figure 7.4: Periodic simulation energy flow diagram

The diagram starts at the top with the equilibrium density and temperature profile gradients. They ultimately supply free energy for the fluctuations. Pointing out of them, the yellow Q_j's extract that energy, channeling it to the density and potential fluctuations. The Q_j's are normalized so that they sum to 100 so that each one represents a percentage of energy brought into the system. Clearly, the $n = 0$ components dominate the energy injection from the equilibrium gradients, and the density injection is much stronger than the temperature injection. The blue T_N and T_T three-wave transfers both go in the direction of $n = 0$ to $n \neq 0$. Dissipation occurs for every fluctuation component and takes all of the injected energy out of the system during the quasi-steady-state stage. Next, the red C_N and C_T transfer channels transfer energy from N and T_e to $v_{\parallel e}$, only at $n \neq 0$, which is the start of the adiabatic response. Actually, $C_T = 0$ because the parallel heat conduction is such a large dissipative factor. Completing the adiabatic response, C_ϕ transfers energy from $v_{\parallel e}$ to ϕ at $n \neq 0$. Finally, T_ϕ shows axial transfer into $n = 0$ ϕ components.

7.2.2 Nonlinear Instability

Fig. 7.4 provides a look at the way energy flows through the system. The nonlinear instability mechanism can be extracted from a subset of the steps in the flow diagram. I provide a reduced diagram in Fig. 7.5 to isolate the essential interactions of the nonlinear instability mechanism. Notice that I focus only on the density fluctuation side (as opposed to the temperature fluctuation side) because it's clear from the numbers in Fig. 7.4 that the density fluctuations are a much stronger drive for the system than the temperature fluctuations. Again, starting at the top, the $n = 0$ potential fluctuations draw energy from the equilibrium density gradient by advection, depositing that energy into the $n = 0$ density fluctuations. Then, those density fluctuations nonlinearly transfer energy into $n \neq 0$ density fluctuations. Next, the adiabatic response acts to transfer some of that energy into $n \neq 0$ potential fluctuations, which finally nonlinearly transfer energy into the $n = 0$ potential fluctuations.
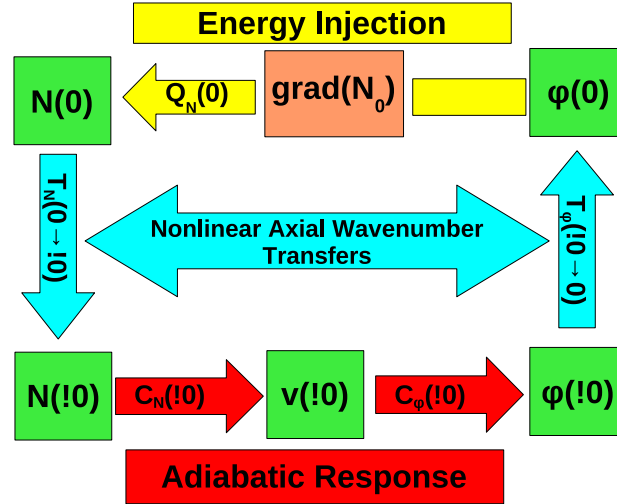

Figure 7.5: Nonlinear instability diagram

Shown in this way, it's clear that the process is self-sustaining. It's also the

dominant process by which the fluctuations get their energy from the equilibrium gradients, which is clear from the fact that $Q_N(n=0)$ comprises 71% of all of the energy injection. Also, the net direction of T_N (from $n=0$ to $n \neq 0$) and its large magnitude support this.

To me at least, this came as a big surprise due to my understanding of the unstable linear eigenmode drive paradigm. Given this paradigm, it seems counterintuitive that energy can be injected into the fluctuations at $n=0$, where only stable linear eigenmodes reside. Furthermore, linear eigenmodes are multi-field objects which have definite phase and magnitude relationships between the different fields. When there are no nonlinearities, the entire eigenmode grows at one particular growth rate, so all of the fields must grow together. The energy dynamics analysis above seems to indicate that the fields don't all grow together or transfer their energy in the same spectral direction.

The reason why regions in wavenumber space where only stable linear eigenmodes exist can actually inject energy into the system is that the linear eigenmodes are nonorthogonal and the nonlinearities can mix the nonorthogonal eigenmodes in complex ways. I don't show the mathematics here, but others have pointed this out and shown it before [CTC98, KT10]. The implication is that stable linear eigenmodes, taken in concert with one another, can inject energy into a system and mix so that the different individual fields act in different ways. Nonorthogonal bases can produce results that are just too complicated to be of use. For these reasons, I abandoned the linear eigenmode decomposition approach early on and chose the simpler decomposition detailed in Chapter 6. Notice that my decomposition actually takes each field separately. I do not attempt to create composit objects of different fields, like others have done using linear eigenvectors [BTG02, TGB02, TG06, TBG06, GTB06, TBH09, KT10, MTK11]. This choice reflects the fact that the different fields can act in different ways.

Now, after I found this curious nonlinear instability, I wondered if others had

previously found this. After all, the equations and the geometry that I use are not new. In fact, a look at Fig. 7.5 reveals that even simpler models like the 3D Hasegawa-Wakatani equations [HW83] contain the proper components to cause the nonlinear instability. And cylindrical simulations of the Hasegawa-Wakatani equations are three decades old (although the original simulations were 2D). My search of the literature reveals that this nonlinear instability was, in fact, identified in 1995. Actually, going even further back, in 1977-1979, Cheng et al. [CO77, CO79] performed 3D turbulence simulations that may have actually been driven by the nonlinear instability. In their work, they identified a dominance of $k_\parallel = 0$ "convective cells [that] are non-linearly excited as a result of mode-coupling of the drift instabilities." It's unclear what equation set they used and what exactly they meant by this mode coupling, but their results seem similar to mine, and it's reasonable to believe that they at least identified the consequences of the nonlinear instability.

In 1995, Biskamp and Zeiler simulated local cylindrical plasma fluid turbulence in the first published use of the 3D Hasegawa-Wakatani equations [BZ95]. Using an energetics analysis, they in fact, correctly identified the nonlinear instability mechanism that drove the $k_\parallel = 0$ structures in their simulations. So the nonlinear instability mechanism is, in fact, not new. Furthermore, others expanded on this original work. Drake et al. showed that elimination of the linear instability by removing the $k_\parallel \neq 0$ components of the linear drive term had virtually no affect on the turbulence [DZB95]. Furthermore, they showed that adding magnetic shear, which also stabilized the linear drift waves, did not stop the turbulence from sustaining itself. Both of these showed that the nonlinear instability could act as a subcritical instability. Additionally, B.D. Scott and others have explore nonlinear drift wave turbulence in a number of different models with different physics effects such as magnetic shear and curvature and found that drift wave turbulence with very long parallel structures tends to sustain itself despite the presence or lack

thereof of linear instabilities [Sco90, Sco92, ZBD96, ZDB97, KMN99, Sco02, Sco03, Sco05].

Nevertheless, it still seems as though no one showed that nonlinear-instability driven drift wave turbulence was relevant to an experiment and not just a simulation artifact. I have attempted to do this here and in published papers [FCU12, FCU13], showing that the simulations driven by the nonlinear instability are validated against experiment (see Sec. 5.3). Also, I will show next that the nonlinear instability is crucial for the simulation to produce experimentally-consistent turbulence.

7.3   n=0 Suppression

I previously introduced the $n = 0$ suppressed simulation in Sec. 5.3, where I discussed the nature of the simulation and some of its statistical properties. I claimed before that this simulation, in which I artificially remove the $n = 0$ components of the density, temperature, and potential fluctuations, eliminates the nonlinear instability. The details of the nonlinear instability mechanism described in the previous section should now make it obvious why removing these components eliminates the nonlinear instability. One may also consider other ways to remove the nonlinear instability while keeping the linear drift wave instability intact. For example, one could remove the $n = 0$ component of the linear drive terms or remove one or more of the nonlinear advection terms, although this would affect quite a bit more than just the nonlinear instability. In any case, my method certainly removes the nonlinear instability mechanism while keeping the linear instability intact, allowing the simulation to act more in the paradigmatic manner.

Rather than showing another diagram of the energy flow for the $n = 0$ suppressed simulation, I present the energy dynamics data in a new, compressed way. That is, I construct a growth rate spectrum from the energy dynamics. I define

the growth rate as:

$$\gamma(\vec{k}) = \frac{\partial E_{tot}(\vec{k})}{\partial t}\bigg|_{lin}\bigg/ \left(2E_{tot}(\vec{k})\right) = \sum_j \left[Q_j(\vec{k}) + D_j(\vec{k})\right]\bigg/ \left(2E_{tot}(\vec{k})\right). \quad (7.1)$$

Recall that $\sum_j C_j(\vec{k}) = 0$, so C_j does not appear in this sum. I also only include the linear contribution to $\frac{\partial E_{tot}(\vec{k})}{\partial t}$ so that the growth rate only involves the energy injection and dissipation at each wavenumber and not the three-wave transfers $(T_j(\vec{k}, \vec{k'}))$. Adding the three-wave transfers would always make this sum about equal to zero in the turbulent quasi-steady state stage of the simulation anyway, rendering this quantity useless. In the linear stage of the simulations, this method reproduces the linear growth rate spectrum. Specifically, this γ is equivalent to the linear growth rate for the fastest growing branch $n = 1$ eigenmodes. I actually used this γ to generate the curves in Figs. 5.1 and 5.2, though I used other methods to confirm the accuracy of this calculation. γ can also be applied to the turbulent stage of the simulation, in which it gives a composit look at the net energy injection into the system at each $\vec{k}$ normalized by the steady-state energy at that given $\vec{k}$.

Fig. 7.6 shows the results of this calculation for three different cases. First, the light blue (cyan) curves represent $\gamma(m)$ for $n = 1$ (the solid line) and $n = 0$ (the dashed line) for the Periodic simulation during the linear exponential growth stage. The $n = 1$ curve is the same as that shown in Figs. 5.1 and 5.2. The $n = 0$ curve, on the other hand, is the linear growth rate of the $n = 0$ linear eigenmodes, which all have negative growth rates of course. The red curves map out γ for the turbulent stage of the Periodic simulation. The $n = 0$ growth rate is *positive* for low m, while the $n = 1$ growth rate is negative for all m. This isn't surprising given the previous section's evidence for $n = 0$ energy injection due to the nonlinear instability, but it is certainly a nice way to show the contrast with the linear growth rate curves. Finally, the green curves are the growth rates for the $n = 0$ suppressed simulation during the "turbulent phase" (recall from
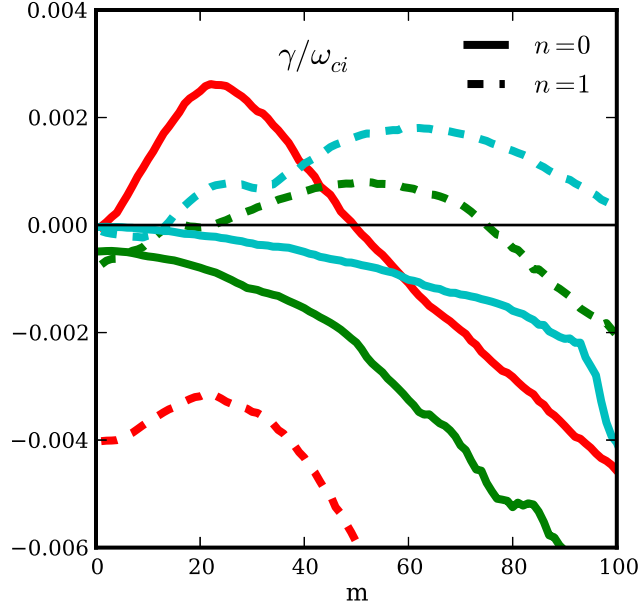
Figure 7.6: Linear vs. nonlinear growth rates

Fig. 5.7 that the fluctuations remain rather coherent, and the state is only weakly turbulent). These growth rates are somewhat similar to the linear growth rates, representative of the expectation under the unstable linear eigenmode paradigm.

Now, one may wonder why there is any $n = 0$ growth rate curve at all for the $n = 0$ suppressed simulation. The reason is because I remove the $n = 0$ components after they are nonlinearly excited. I allow the nonlinearities to transfer energy into the $n = 0$ components at each time step and then I save the data. The energy, by the way, is transferred from $n = 1$ to $n = 0$ modes as in the paradigmatic process. Then, I remove these $n = 0$ components before the equations are evolved again. So there are small values for these $n = 0$ components that come out in the data, but are not used to evolve the equations. This allows construction of the $n = 0$ growth rate curve. Furthermore, notice that the $n = 0$ suppressed simulation growth rates do not exactly match the linear growth rates. The reason for this is that the nonlinearities change the structures and phases between the

fields. Or to put it another way, they excite slower growing or damped eigenmodes that lessen the effect of the most unstable eigenmodes. This is consistent with the linear instability paradigm.
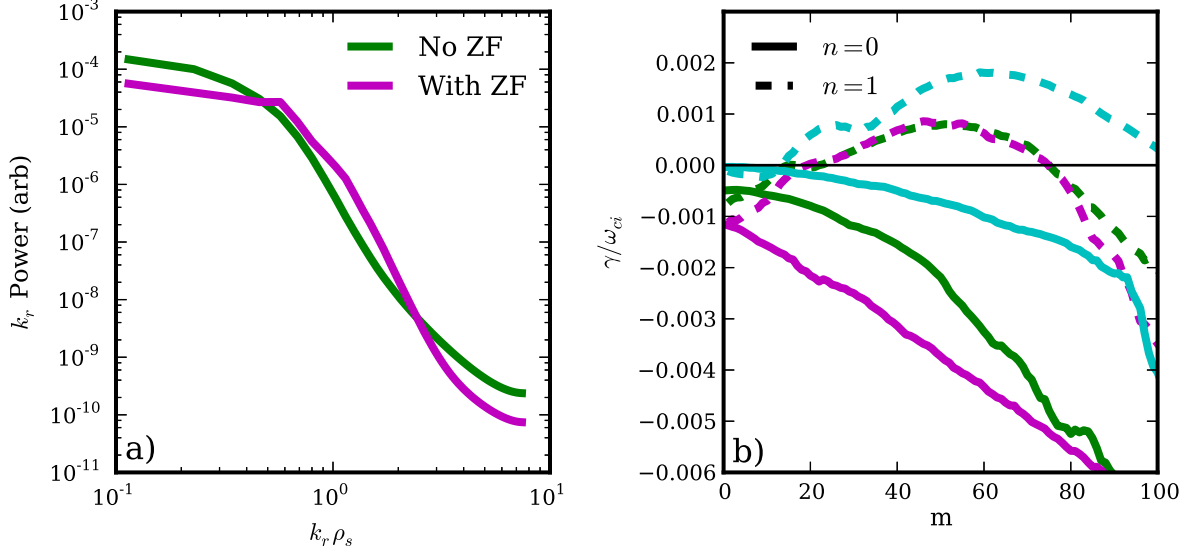

Figure 7.7: Zonal flow affect on spectra and growth rate

Finally, one might notice that manually removing all of the $n = 0$ fluctuation components means that the zonal flows ($n = 0, m = 0$ component of ϕ) are also removed. Zonal flows are often seen as being an important saturation mechanism for turbulence by either shearing the turbulent eddies [BDT90] or by exciting stable eigenmodes [MTK12]. They are often considered to provide the most important nonlinear interactions to plasma turbulence. So one might naively think that their removal in the $n = 0$ suppressed simulation causes the removal of the nonlinear instability. I say "naively" because the nonlinear instability mechanism outlined in Fig. 7.5 doesn't depend upon zonal flows. But to prove this and to explore the real affect of the zonal flows, I have rerun the $n = 0$ suppressed simulation without removing the zonal flows. I still remove all of the $n = 0$ components of the density and temperature fluctuations and all of the $n = 0, m \neq 0$ components

of ϕ, but I leave the zonal flow component intact. I show some comparisons of the two simulations in Fig. 7.7. In Fig. 7.7 a), I show the k_r spectrum of the two simulations, revealing that the zonal flows cause radial wavenumber transfers from low k_r to medium k_r. This is a simple consequence of a three-wave interaction between the dominant low k_r structures and the zonal flows which have finite k_r. This interaction causes a slight saturation effect because the medium k_r modes have lower growth rates than the low k_r modes, and the overall saturation level is depressed by about a factor of 2 when I retain the zonal flows.

Nevertheless, the zonal flows don't cause the nonlinear instability, which is evident from Fig. 7.7 b) where the nonlinear growth rates of the two simulations are shown along with the linear growth rates. Recall from Fig. 7.6 how different the growth rates look when the nonlinear instability is present. The simulation with the zonal flows is qualitatively similar to the simulation without the zonal flows, but as expected, the growth rates with the zonal flows are less than or equal to the growth rates without the zonal flows. Interestingly, the zonal flows only affect the growth rates at $n = 1$ at very low and very high m, but they affect the $n = 0$ growth rates mostly at medium m. Anyhow, the zonal flows don't affect the nonlinear instability, and they also have a relatively weak affect on turbulent saturation compared to some other types of turbulence like ITG turbulence [DBB00, HDC03].

CHAPTER 8

Energy Dynamics for the Non-periodic Simulations

I turn my focus in this chapter to the simulations with non-periodic axial boundary conditions; namely the Dirichlet, Neumann, and Sheath simulations. I showed in Sec. 5.1 that the linear properties of these simulations are rather different from the Periodic simulation and from one another. However, the statistical turbulent properties of the four simulations are all quite similar (Sec. 5.3). This, combined with the observation that the turbulence in the Periodic simulation self-organizes and drives itself by nonlinear instability, points to the conclusion that the axial boundary conditions have little affect on the nonlinear instability or the energy dynamics in general. Nevertheless, additional supporting evidence for this claim can provide confirmation regarding the robustness of the nonlinear instability. I therefore explore the energy dynamics of the non-periodic simulations in this chapter, attempting to differentiate the nonlinear dynamics from the linear ones.

8.1   Fourier Decomposing Non-periodic Functions

To my knowledge, nobody has considered the affect of non-periodic axial boundary conditions on this nonlinear instability in a straight magnetic field. But this is a critical extension of the topic because in the real world, linear plasma devices don't have periodic boundary conditions. Additionally, the nonlinear instability seems to crucially depend on axial wavenumber dynamics, which should be affected by

the axial boundary conditions. It is perhaps surprising then that nobody has taken up this line of research.

On the other hand, it may not be so surprising given that the non-periodicity can cause interpretation issues regarding the linear vs. the nonlinear instability. To clarify, in the periodic case, the linear eigenmodes are sinusoildal with integer axial mode numbers. And all of the unstable eigenmodes have $|n| \geq 1$. So any energy injection into $n = 0$ fluctuations is a clear indication that the unstable linear eigenmodes are not responsible for such injection. In the non-periodic cases, the linear eigenmodes are not necessarily sinusoidal (see Fig. 5.2 b)) and if they are, they certainly don't have integer mode numbers. Fourier decompositions of the non-periodic unstable eigenmodes yields finite $n = 0$ Fourier coefficients. This can muddle interpretation of energy injection into $n = 0$ fluctuations during the turbulent simulation phase. It seems as though a linear eigenmode decomposition may fix this problem, but these decompositions are difficult to perform in practice, and more importantly, decompositions with highly non-normal bases aren't guaranteed to yield interpretable results. So I proceed with the spectral energy dynamics on non-periodic simulations and show that the results are less clear-cut than those of the Periodic simulation, but nevertheless, rather conclusive in that the nonlinear instability still dominates.

First, however, I raise another problem regarding spectral energy dynamics and spectral analysis in general. That problem is Gibbs phenomena. Fourier basis functions are continuous and periodic, so Fourier decomposing discontinuous or non-periodic functions leads to Gibbs phenomena. One of the significant results of this is the slow convergence of Fourier reconstructions to the original signal. Mathematically, I can take a discrete signal with the following Fourier decomposition:
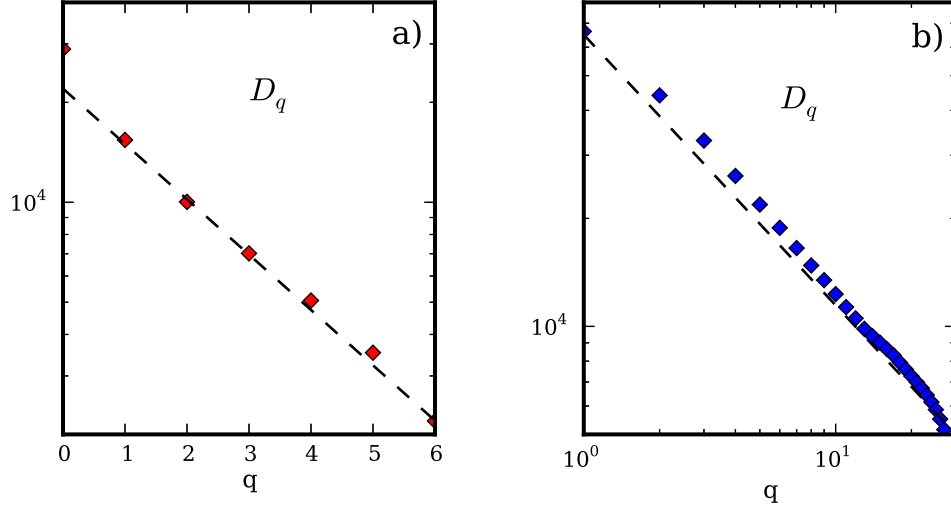
Figure 8.1: Convergence of Fourier reconstructions

$$f(x) = \sum_{k=-Q}^{Q} \hat{f}_k e^{2\pi i k x}, \qquad (8.1)$$

where the $\hat{f}_k$ are ordered in the sum by the size of their absolute value with $\hat{f}_0$ being the largest Fourier coefficient. The Fourier reconstruction of order $q < Q$ is then:

$$g_q(x) = \sum_{k=-q}^{q} \hat{f}_k e^{2\pi i k x} \qquad (8.2)$$

There are several types of convergences of the g_q, one of which is the $L1$ norm. Defining the difference between the original signal and the Fourier reconstruction of order q as $D_q = \sum_x |f(x) - g_q(x)|$, I can look at the convergence of D_q as a function of q. For continuous periodic signals, D_q converges exponentially, while it only converges algebraically (power law) for non-periodic or discontinuous signals.

As an example, I have plotted D_q for the Periodic and Sheath simulations in Fig. 8.1. The Periodic simulation in Fig. 8.1 a) converges exponentially, while the Sheath simulation in Fig. 8.1 b) converges algebraically. Now in this figure, even

77

though the x-axis label q indicates the mode with the qth largest amplitude by construction of Eq. 8.2, it also happens to correspond to the axial mode number n for all but the last few q. In other words, in both simulations, most of the energy is contained in $n = 0$ modes followed by $n = 1$ modes and so on. So I should still be able to focus on the $n = 0$ and $n = \pm 1$ mode numbers in the energy dynamics data, but they will not contain as much of the dynamics as they do for the Periodic case.

8.2 Energy Dynamics Results

The simplest way to view the vast quantities of energy dynamics information is through the effective growth rate defined in Eq. 7.1. So in Fig. 8.2, I show the growth rates for all of the simulations. In Fig. 8.2 a), I plot the growth rates during the turbulent phases of all five simulations (see Fig. 5.7 for the color code). Again, I break up the $n = 0$ and $n = 1$ components and don't show the $n \geq 2$ growth rates. Notice that the Periodic, Dirichlet, Neumann, and Sheath simulations all have quite similar growth rates, especially at $n = 0$. Their $n = 1$ growth rates have similar m dependencies, but somewhat different magnitudes, and the $n = 1$ growth rates are all negative except for a small region in the Dirichlet curve, which is marginal. Contrast these with the $n = 0$ suppressed simulation, which recall, is dominated by the linear instability. These growth rates certainly indicate that the same kind of processes occur for the four similar simulations regardless of axial boundary conditions – namely, the nonlinear instability process. This isn't too surprising given the similarity of the turbulent statistics of the four simulations (Fig. 5.7).

It is also instructive to compare the nonlinear turbulent growth rates against the linear growth rates as I did for the Periodic simulation in Fig. 7.6. I do this for the non-periodic simulations in Figs. 8.2 b)-d). The black curves in these

78
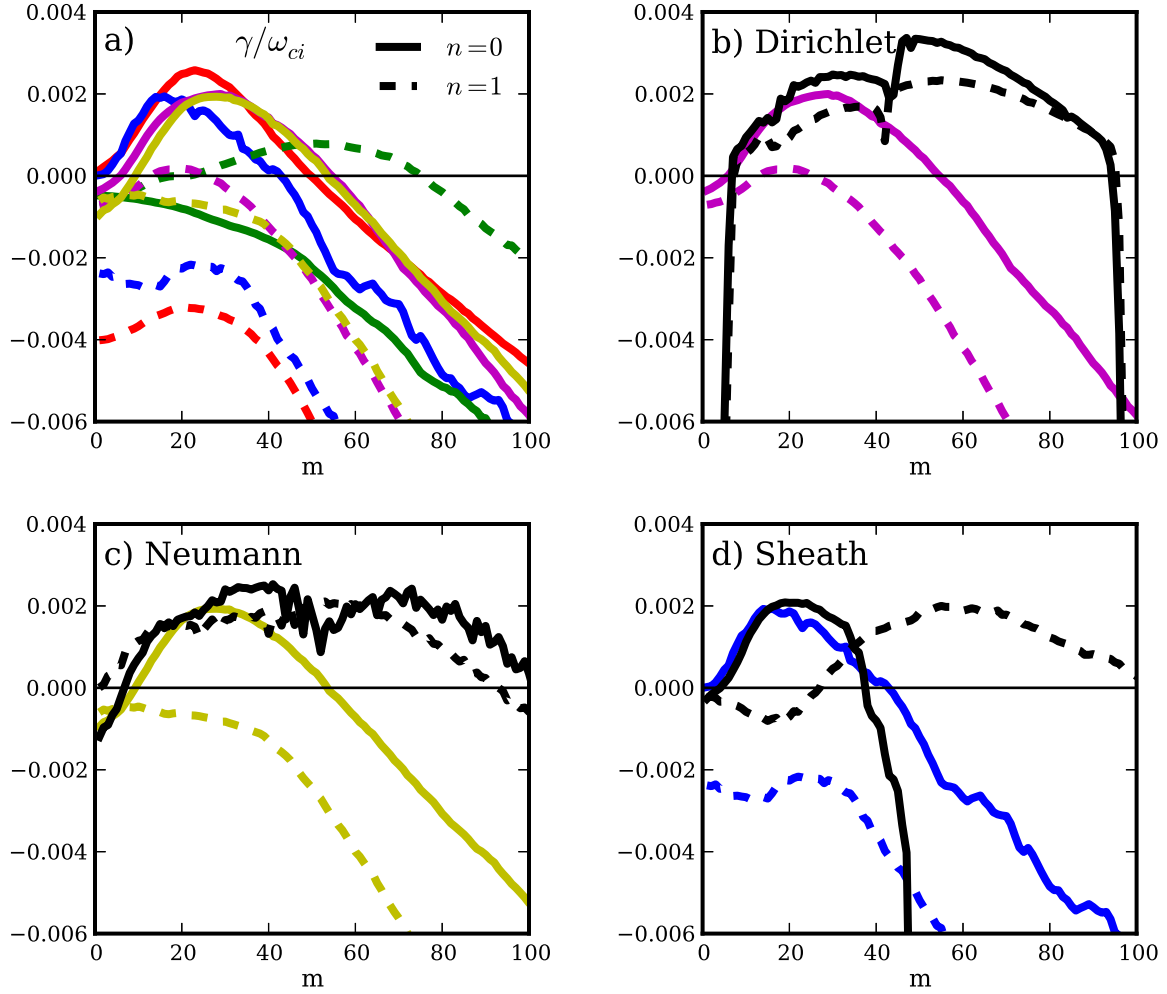
Figure 8.2: Linear and nonlinear growth rates of all simulations

figures are the linear growth rates for each respective simulation. For example, the solid black line in Fig. 8.2 b) corresponds to the $n = 0$ linear growth rate of the Dirichlet simulation. The dashed black line in this figure corresponds to the $n = 1$ growth rate of the Dirichlet simulation. Note that the linear growth rates come from the same data as that used in Fig. 5.2, but these are decomposed in m and n, while those were simply decomposed in m.

Now all three of these simulations (Dirichlet, Neumann, and Sheath) have a lot of similarity, especially the Dirichlet and Neumann simulations. The $n = 1$ growth rate curves for all three simulations are all qualitatively different between the linear and the nonlinear stage. For the most part, the $n = 1$ linear growth rates are always positive, while the $n = 1$ nonlinear growth rates are always negative. The $n = 0$ linear growth rates for the Dirichlet and Neumann simulations are similar to the $n = 1$ linear growth rates because the linear eigenmode structures contain roughly equal parts $n = 0$ and $n = 1$ and the density-potential phases are set by the linear drift-wave physics. The $n = 0$ and $n = 1$ Sheath simulation linear growth rates are quite different because the linear eigenmodes actually undergo a bifurcation at $m \sim 40$. All $m < 40$ Sheath linear eigenmodes have shapes like that in Fig. 5.2 b), which are even about the axial midpoint. However, all $m > 40$ linear eigenmodes have shapes that are odd about the axial midpoint. The CWM has even and odd solution branches whose growth rates cross at $m \sim 40$, causing this seemingly odd behavior.

In any case, it is interesting that the $n = 0$ linear and nonlinear growth rates for these three simulations are nearly equal for $m < 50$. However, they are not at all similar for $m > 50$. Does this low m region of similarity indicate that the linear instability dominates these simulations? Based on Fig. 8.2 a), the $m > 50$ region, and the $n = 1$ dissimilarity, I would say that the nonlinear instability is still the dominant player. However, it's not conclusive either way, and it's possible that in some complicated way, the linear and nonlinear physics are somewhat similar in this region. This is the problem of using Fourier decompositions rather than linear eigenmode decompositions, although as I stated before, there's no guarantee that an eigenmode decomposition would yeild anything more conclusive because of the eigenmode nonorthogonality. Eigenmode nonorthogonality is the real culprit to all of the difficulties, in fact. It causes the nonlinear instability, but it also makes it difficult to identify in some cases. Therefore, I try to devise a way around this

in the next section.

8.3 Linear vs Nonlinear Structure Correlation

To try to sort out the problem of linear vs. nonlinear instability in a non-normal linear system, I propose the following method. First, imagine the case where a simulation is dominated by a linear instability. Then, the fastest growing linear eigenmode dominates the system, nonlinearly transfering some energy to more weakly unstable or even stable eigenmodes. In this case, a large portion of the energy should remain in the fastest growing linear eigenmode [HTJ11]. In the alternative case where a nonlinear instability is dominant, the linear eigenmode should have little bearing on the structure of the turbulence and therefore little energy should be contained in this eigenmode. Therefore, a reasonable gauge of whether a linear or nonlinear instability dominates a system is the fraction of energy in a turbulent system that is contained in the fastest growing linear eigenmode. This may be calculated by projecting the fastest growing eigenmode onto the turbulent state.

Formally, in my model, I fully describe the turbulent state by four independent fields, which I can appended into a single vector of the spatio-temporal field functions: $f_{turb}(\vec{r}, t) = \{N(\vec{r}, t), T_e(\vec{r}, t), \nabla_\perp \phi(\vec{r}, t), v_{\|e}(\vec{r}, t)\}$. This vector may be decomposed in a complete basis:

$$f_{turb}(\vec{r}, t) = \sum_{i,m} c_{i,m}(t) \psi_{i,m}(r, z) e^{im\theta}, \tag{8.3}$$

where $\psi_{i,m}(r, z)$ are time-independent spatial complex basis functions of the form $\psi_{i,m}(r, z) = \{n_{i,m}(r, z), t_{i,m}(r, z), \nabla_\perp \phi_{i,m}(r, z), v_{i,m}(r, z)\}$, and $c_{i,m}(t)$ are the complex time-dependent amplitudes. I have explicitly imposed a Fourier bases for the θ dependence of the basis functions. The total number of linearly independent

basis functions is the number of total grid points used in the simulation times the number of independent fields, which is four in this case. Now, $\psi_{i,m}(r,z)$ can be any linearly independent set of functions and need not be the linear eigenfunctions of the system. In fact, I want to use orthogonal basis functions, ruling out the linear eigenfunctions. However, it is quite useful to set $\psi_{0,m}(r,z)$ to the fastest growing linear eigenmode because this is the structure of interest that is to be projected onto the turbulence. The other $\psi_{i\neq 0,m}(r,z)$ comprise the remainder of the orthonormal basis, and they must be different from the remaining linear eigenfunctions in order to complete the orthogonal basis. It isn't necessary for the purpose of this study to actually compute these other basis functions, but if I were to compute them, I would probably start with all of the linear eigenmodes and perform a Gram-Schmidt orthogonalization procedure, making sure to start with the fastest growing eigenmode in order to preserve it. Using this procedure, Hatch et al. [HTJ11] found that a significant fraction ($\sim$ 50%) of the energy in a turbulent state of ITG turbulence was contained in the fastest growing linear eigenmode at each perpendicular wavenumber. Such a result, however, doesn't require knowledge of the other basis functions, and thus I don't compute them here.

Now, to compute the fraction of energy in the fastest growing eigenmode to the total energy, I first define an inner product that is energetically meaningful and that sets the orthonormality of the basis functions:

$$\langle \psi_{i,m}, \psi_{j,m} \rangle = \int w \psi_{i,m}^* \cdot \psi_{j,m} dV = \delta_{i,j}. \tag{8.4}$$

The weighting w is such that $\langle f_{turb}, f_{turb} \rangle = E_{turb}$. Now from Eqs. 8.3 and 8.4, $\langle f_{turb}, f_{turb} \rangle = E_{turb} = \sum_{i,m} |c_{i,m}|^2$ and $\langle f_{turb,m}, f_{turb,m} \rangle = E_{turb,m} = \sum_i |c_{i,m}|^2$. Then, the amount of energy contained in the fastest growing mode (for each m) is given by the square of the projection of the mode onto the turbulence: $E_{0,m} = |\langle \psi_{0,m}, f_{turb,m} \rangle|^2 = |c_{0,m}|^2$. The ratio $R_m = E_{0,m}/E_{turb,m}$ is a measure of

the fraction of turbulent energy contained in the fastest growing linear eigenmode.

Of course, $E_{turb,m}$ is easily calculated from the turbulent state, but $E_{0,m}$ in the turbulent state can only be found with knowledge of the fastest growing eigenfunction. The fastest growing eigenfunction, though, can be found easily by running a simulation from a random or turbulent state with all of the nonlinearities removed from the model equations. After some time, the fastest growing eigenfunctions will come to dominate the fluctuation structure. Then, a Fourier decomposition in m space will separate the fastest growing eigenfunctions at each m, including the real and imaginary part of the eigenfunctions (up to a time dependent complex constant, which is removed by normalizing the eigenfunction). I can then project the eigenfunctions onto the turbulent state with the inner product defined in Eq. 8.4, giving $E_{0,m}$.

I do this and show the ratio R_m in Fig. 8.3 for the five simulations. For the most part, the simulations other than the $n = 0$ suppressed one have a small value of the ratio ($R_m < 0.3$) for all m. This confirms that the turbulence largely self-organizes without regard to the linear physics in the four other simulations. The one exception is the Dirichlet simulation for $m > 50$, which has $R_m \sim 0.5$. This is quite the unexpected result, and I can't explain it based on any of the other evidence. Most of the energy in this and the other simulations, however, is at low m (Fig. 7.1), so these larger m eigenmodes don't make a large impact on the overall structure of the turbulence.

In fact, R_m is below 0.1 for $m < 40$ for the periodic, Dirichlet, and Neumann simulations, precisely the area where $n = 0$ structures dominate the energy spectrum. This answers the question posed in the previous section regarding the similarity in the $n = 0, m < 40$ linear and nonlinear growth rates for the Dirichlet and Neumann simulations. The fastest growing linear eigenmodes do not significantly drive the turbulence in this region. The nonlinear instability does.

On the other hand, the fastest growing eigenfunctions make up a significant

fraction of the energy in the $n = 0$ suppressed simulation. Where the linear drift wave instability (and the turbulent growth rate) is the strongest (at $m \sim 50$), $R_m \sim 0.5$. The linear physics controls the $n = 0$ suppressed simulation, and the linear eigenmode structure certainly asserts itself in the turbulence, but only to a degree (50%).

The Sheath simulation is the most difficult to analyze because it has more linear eigenmode dominance at low m than the other simulations. R_m is still only about 0.25 there. While this isn't at the level of the $n = 0$ suppressed simulation or the Hatch et al. gyrokinetic ITG simulation [HTJ11], it still might be significant. It appears that the linear instability never completely disappears from any of the simulations, and the level to which it acts on the turbulence differs between the different simulations. The Sheath simulation is driven more by its linear instability than all of the others except for the $n = 0$ suppressed simulation, indicating a possibly important role for the CWM in LAPD, though LAPD doesn't have such simple boundary conditions. However, the turbulence statistics of the Sheath simulation are so similar to those of the other simulations (Sec. 5.3) that $R_m \sim 0.25$ probably isn't significant enough to say that the linear instability dominates.

8.4 Nonlinear Saturation Levels

A common topic of plasma turbulence is the prediction of the saturation level of turbulence. Generally, such predictions are based off of linear properties, however, a dominant nonlinear instability should have an affect on the level at which the turbulence saturates. One theory – mixing length theory – based on linear drift waves predicts that the saturation level should be about $\gamma/k_\perp^2$ where γ and $k_\perp$ are the growth rate and perpendicular wavenumber of the fastest growing linear eigenmode [Hor90]. Turbulence driven by a nonlinear instability may saturate at
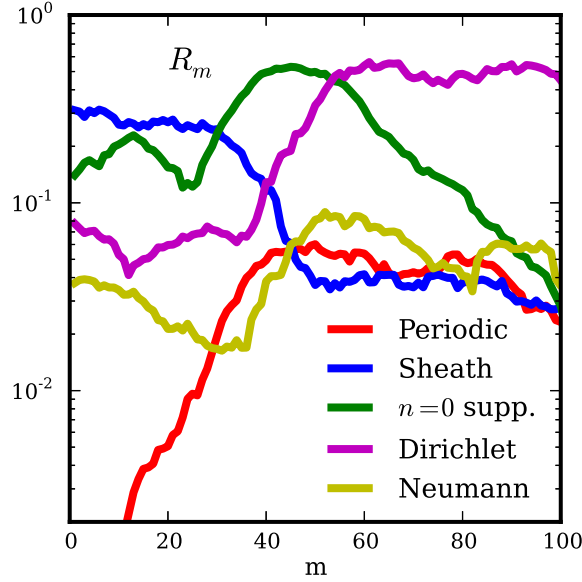
Figure 8.3: Energy fraction contained in the most unstable eigenmodes

some other level, which seems probable given Fig. 5.7, which shows that the $n = 0$ suppressed simulation saturates at a lower level than the simulations driven by the nonlinear instability.

Mixing length theory provides an estimate for the turbulence saturation level where only properties of the linear eigenmodes are known. This can be quite useful to find scaling relations, and allows prediction without direct numerical simulation. Therefore, I develop a corresponding estimate based on the drift wave turbulence driven by the nonlinear instability that I have described. Now, it is quite difficult to predict a saturation level based on a nonlinear mechanism when nonlinear simulation results are not available. However, as suggested in Ref. [CO79], and as seen in Fig. 5.4 b), it appears that the turbulence begins to saturate when the amplitude of the $n = 0$ field components becomes equal to the $n = 1$ field components. At this point, the strongest nonlinear interaction term catches up to the linear terms, bringing about the onset of saturation. However, the nonlinear instability really doesn't become important up until this point, which

85

is why saturation occurs only when values are a few times higher than this point. Therefore, this crossing point can only be seen as a rough approximation for the saturation level, and more work will be needed to improve upon this calculation.

Now in order to find the crossing point amplitude, notice from Fig. 5.4 b), that before the components become equal, in the linear phase of the simulation, the $n = 0$ components seem to have twice the growth rate of the $n = 1$ components. This indicates that the $n = 0$ components are driven nonlinearly (parametrically). Furthermore, both are exponentially growing in the linear phase. It is possible then to use only linear eigenmode knowledge to compute the level at which the $n = 0$ and $n = 1$ components become equal as long as both start at small amplitudes and experience a few e-foldings before saturating. I now derive an approximate scaling relation for the crossing point.

First, to simplify matters, I use a local model in which each linear eigenmode can be identified by its wavevector $\vec{k} = (k_r, k_\theta, k_z)$. In reality, the number of eigenvectors at each $\vec{k}$ is equal to the number of fields (4 in my case), but I ignore all but the fastest growing one, which is the only important one in the linear phase of the simulation. So to start, I write the evolution of each eigenmode component during the linear phase of the simulation as:

$$\frac{\partial A_{\vec{k}}}{\partial t} = -i\omega_{\vec{k}} A_{\vec{k}} + T_{\vec{k}} \tag{8.5}$$

where $\omega = \omega_{R,\vec{k}} + i\gamma_{\vec{k}}$ and the nonlinear transfer term $T_{\vec{k}}$ equal to:

$$T_{\vec{k}} = \sum_{\vec{k}'} (k_r k_\theta' - k_\theta k_r') A_{\vec{k}'} \phi_{\vec{k}-\vec{k}'} \tag{8.6}$$

This equation is essentially the same as Eq. 6.21 but with eigenmodes instead of energies. It's easiest to see that the linear terms take the simple $-i\omega A_{\vec{k}}$ form by neglecting the nonlinear term and noticing that the linear eigenmode has to

evolve with its characteristic frequency ω and growth rate γ. Now the $n = 1$ fastest growing eigenmode curve, which has $m \sim 60$, evolves as:

$$\frac{\partial A_d}{\partial t} = -i\omega_d A_d \tag{8.7}$$

where A_d represents the fastest growing $n = 1, m \sim 60$ linear drift wave structure with time-dependent amplitude (d is shorthand for the wavevector of this eigenmode). Note that I have made the assumption that in the linear phase of the simulation, the linear term dominates the nonlinear term, which is quadratic in two small quantities. The solution of this equation is:

$$A_d(t) = A_d(0)e^{-i\omega_d t}. \tag{8.8}$$

On the other hand, the $n = 0$ mode has much smaller amplitude than the linear drift wave during the linear simulation phase, meaning that the nonlinear term can be comparable to or larger than the linear term. Specifically, the evolution equation for the $n = 0$ "convective cells" is:

$$\frac{\partial A_c}{\partial t} = -i\omega_c A_c + \sum_{\vec{k}'}(k_{rc}k'_\theta - k'_r k_{\theta c})A_{\vec{k}'}\phi_{c-\vec{k}'}. \tag{8.9}$$

Now, the convective cells that grow the fastest have $m \sim 0$. This is clear by noting that the largest term in the sum should have $\vec{k}' = d$ and $c \sim 0$. Using the symbol M_{cd} for the wavevector difference $k_{rc}k_{\theta d} - k_{rd}k_{\theta c}$ and noting that $\phi_{-d} = \phi_d^* \sim A_d^*$,

$$\frac{\partial A_c}{\partial t} \approx -i\omega_c A_c + M_{cd}|A_d|^2. \tag{8.10}$$

Plugging in Eq. 8.8 into the A_d in this equation, and then solving this differential equation for $A_C(t)$ results in:

$$A_c(t) = A_c(0)e^{-i\omega_c t} + \frac{M_{cd}|A_d(0)|^2}{2\gamma_d + i\omega_c}\left(e^{2\gamma_d t} - e^{-i\omega_c t}\right). \qquad (8.11)$$

Now a large simplifying approximation is that $\omega_c = 0$. I essentially take the linear eigensystem of these convective cells to have zero axial wavenumber, zero frequency and growth rate, near-zero azimuthal wavenumber, and radial wavenumber about twice that of the drift wave radial wavenumber. All of these assumptions are confirmed by the spectra of the convective cells and drift waves (not shown here). Also, these mean that $k_{rc}k_{\theta d} \gg k_{rd}k_{\theta c}$, so that $M_{cd} \approx k_{rc}k_{\theta d}$ Then,

$$A_c(t) = A_c(0) + \frac{k_{rc}k_{\theta d}|A_d(0)|^2}{2\gamma_d}\left(e^{2\gamma_d t} - 1\right). \qquad (8.12)$$

At the time (t_f), when the amplitudes of the drift waves and convective cells equal one another, the initial perturbation $A_c(0)$ is much smaller than the second term on the right hand side of Eq. 8.12 and can therefore be neglected when looking at large times. So, setting the amplitude of $A_d(t_f)$ from Eq. 8.8 to the amplitude of $A_c(t_f)$ from Eq. 8.12 and performing some algebra, the result is:

$$|A_c(t_f)| = |A_d(t_f)| = \frac{2\gamma_d}{k_{rc}k_{\theta d}}. \qquad (8.13)$$

The factor of two probably isn't significant given the approximations that went into this result, but the scalings of the drift wave growth rate, the drift wave azimuthal wavenumber, and the convective cell radial wavenumber are. The result is very similar to the mixing length result except that the wavenumbers of interest are from both the drift waves and the convective cells rather than from just the drift waves. Putting in LAPD values for this relation gives that the crossing level amplitude should be about 0.05. This is consistent with the amplitude at which the simulations begin to saturate, as can be seen in Fig. 5.4 a). Again, though, the ultimate saturation level is somewhat larger than this, and it's not clear if that

ultimate saturation level can be completely predicted without direct numerical simulation.

One last point I want to make involves the $n \geq 2$ curves in Fig. 5.4 b). These curves all appear to grow at the same growth rate as the $n = 1$ curve during the linear stage of the simulation. This may seem odd because the linear growth rates of the eigenmodes with these higher axial mode numbers are much less than the growth rate of the fastest $n = 1$ eigenmode. Furthermore, if these modes were to be pumped nonlinearly (parametrically), one might expect them to grow with twice the growth rate of the $n = 1$ curve just like the $n = 0$ curve does. In fact, the $n \geq 2$ curves are pumped nonlinearly. A look at the spectra (not shown) reveals that all of the $n \geq 2$ modes have $k_r - k_\theta$ spectra just like that of the $n = 1$ mode. So this means that the nonlinear interaction that drives the $n \geq 2$ modes involves the fastest growing $n = 1$ linear eigenmode beating against an eigenmode that has $k_r \sim k_\theta \sim 0$. This second eigenmode has close to zero growth rate, meaning that the $n \geq 2$ modes will only grow at the same rate as the fastest growing $n = 1$ linear eigenmode and not at twice its growth rate. It's difficult to guess this *a priori* due to the complexity of the nonlinear transfer term, so it seems that simulation results have to provide the evidence for this.

CHAPTER 9

Finite Mean Flow Simulations

CHAPTER 10

Conclusion

APPENDIX A

The BOUT++ Code

A.1 The Object-Oriented Fluid Framework

A.2 Explicit Finite Differences

A.3 The Physics Inputs

APPENDIX B

Grid Convergence

References

[Ara66]   A. Arakawa. "Computational Design for Long-Term Numerical Integration of the Equations of Fluid Motion." *J. Computational Physics*, **1**:119–143, 1966.

[BCR93]   H. L. Berk, R. H. Cohen, D. D. Ryutov, Yu. A. Tsidulko, and X. Q. Xu. "Electron temperature gradient induced instability induced in tokamak scrape-off layers." *Nuclear Fusion*, **33**:263, 1993.

[BDT90]   H. Biglari, P. H. Diamond, and P. W. Terry. "Influence of sheared poloidal rotation on edge turbulence." *Phys. Fluids B*, **2**:1, 1990.

[Bra65]   S. I. Braginskii. "Transport processes in a plasma." In M A Leontovich, editor, *Reviews of Plasma Physics*, volume 1, pp. 205–311. Consultants Bureau, New York, 1965.

[BRT91]   H. L. Berk, D. D. Ryutov, and Yu. A. Tsidulko. "Temperature-gradient instability induced by conducting end walls." *Phys. Fluids B*, **3**:1346, 1991.

[BTG02]   D. A. Baver, P. W. Terry, R. Gatto, and E. Fernandez. "Nonlinear stability and instability in collisionless trapped electron mode turbulence." *Phys. Plasmas*, **9**:3318, 2002.

[BZ95]   D. Biskamp and A. Zeiler. "Nonlinear Instability Mechanism in 3D Collisional Drift-Wave Turbulence." *Phys. Rev. Lett.*, **74**:706, 1995.

[CBS95]   S. J. Camargo, D. Biskamp, and B. D. Scott. "Resistive drift-wave turbulence." *Phys. Plasmas*, **2**:48, 1995.

[Che06]   F. F. Chen. *Introduction to Plasma Physics and Controlled Fusion*. Springer, 2006.

[CO77]   C. Z. Cheng and H. Okuda. "Formation of convective cells, anomalous diffusion, and strong plasma turbulence due to drift instabilities." *Phys. Rev. Lett.*, **38**:708, 1977.

[CO79]   C. Z. Cheng and H. Okuda. "Theory and numerical simulations on collisionless drift instabilities in three dimensions." *Nuclear Fusion*, **18**:587, 1979.

[CTC98]   S. J. Camargo, M. K. Tippett, and I. L. Caldas. "Nonmodal energetics of resistive drift waves." *Phys. Rev. E*, **58**:3693, 1998.

[DBB00]   A. M. Dimits, G. Bateman, M. A. Beer, B. I. Cohen, W. Dorland, G. W. Hammett, C. Kim, J. E. Kinsey, M. Kotschenreuther, A. H. Kritz, L. L. Lao, J. Mandrekas, W. M. Nevins, S. E. Parker, A. J. Redd, D. E. Shumaker, R. Sydora, and J. Weiland. "Comparisons and Physics Basis of Tokamak Transport Models and Turbulece Simulations." *Phys. Plasmas*, **7**:969, 2000.

[DUX09]   B. D. Dudson, M. V. Umansky, X. Q. Xu, P. B. Snyder, and H. R. Wilson. "BOUT++: A framework for parallel plasma fluid simulations." *Computer Physics Communications*, pp. 1467–1480, 2009.

[DZB95]   J. F. Drake, A. Zeiler, and D. Biskamp. "Nonlinear Self-Sustained Drift-Wave Turbulence." *Phys. Rev. Lett.*, **75**:4222, 1995.

[FCU12]   B. Friedman, T. A. Carter, M. V. Umansky, D. Schaffner, and B. Dudson. "Energy dynamics in a simulation of LAPD turbulence." *Phys. Plasmas*, **19**:102307, 2012.

[FCU13]   B. Friedman, T. A. Carter, M. V. Umansky, D. Schaffner, and I. Joseph. "Nonlinear instability in simulations of Large Plasma Device turbulence." *Phys. Plasmas*, 2013.

[GTB06]   R. Gatto, P. W. Terry, and D. A. Baver. "Nonlinear damping of zonal modes in anisotropic weakly collisional trapped electron mode turbulence." *Phys. Plasmas*, **13**:022306, 2006.

[HDC03]   C. Holland, P. H. Diamond, S. Champeaux, E. Kim, O. Gurcan, M. N. Rosenbluth, G. R. Tynan, N. Crocker, W. Nevins, and J. Candy. "Investigations of the role of nonlinear couplings in structure formation and transport regulation: experiment, simulation, and theory." *Nuclear Fusion*, **43**:761, 2003.

[Hor90]   W. Horton. *Nonlinear drift waves and transport in magnetized plasma.* North-Holland, 1990.

[HTJ11]   D. R. Hatch, P. W. Terry, F. Jenko, F. Merz, and W. M. Nevins. "Saturation of Gyrokinetic Turbulence through Damped Eigenmodes." *Phys. Rev. Lett.*, **106**:115003, 2011.

[Hut02]   I. H. Hutchinson. *Principles of Plasma Diagnostics.* Cambridge University Press, 2002.

[HW83]   A. Hasegawa and M. Wakatani. "Plasma Edge Turbulence." *Phys. Rev. Lett.*, **50**:682–686, 1983.

[KMN99]   S. B. Korsholm, P. K. Michelsen, and V. Naulin. "Resistive drift wave turbulence in a three-dimensional geometry." *Phys. Plasmas*, **6**:2401, 1999.

[KT10]   J.-H. Kim and P. W. Terry. "Energetic study of the transition to nonlinear state in two-dimensional electron temperature gradient fluid turbulence." *Phys. Plasmas*, **17**:112306, 2010.

[LRH12]   J. Loizu, P. Ricci, F. Halpern, and S. Jolliet. "Boundary conditions for plasma fluid models at the magnetic presheath entrance." *Phys. Plasmas*, **13**:122307, 2012.

[MTK11]   K. D. Makwana, P. W. Terry, J. H. Kim, and D. R. Hatch. "Damped eigenmode saturation in plasma fluid turbulence." *Phys. Plasmas*, **18**:012302, 2011.

[MTK12]   K. D. Makwana, P. W. Terry, and J. H. Kim. "Role of stable modes in zonal flow regulated turbulence." *Phys. Plasmas*, **19**:062310, 2012.

[PUC10a]   P. Popovich, M. V. Umansky, T. A. Carter, and B. Friedman. "Analysis of plasma instabilities and verification of BOUT code for linear plasma device." *Phys. Plasmas*, **17**:102107, 2010.

[PUC10b]   P. Popovich, M. V. Umansky, T. A. Carter, and B. Friedman. "Modeling of plasma turbulence and transport in the Large Plasma Device." *Phys. Plasmas*, **17**:122312, 2010.

[RR10]   B. Rogers and P. Ricci. "Low-frequency turbulence in a linear magnetized plasma." *Phys. Rev. Lett.*, **104**:225002, 2010.

[SC03]   A. N. Simakov and P. J. Catto. "Drift-ordered fluid equations for field-aligned modes in low-β collisional plasma with equilibrium pressure pedestals." *Phys. Plasmas*, **10**:4744, 2003.

[Sco90]   B. D. Scott. "Self-Sustained Collisional Drift-Wave Turbulence in a Sheared Magnetic Field." *Phys. Rev. Lett.*, **65**:3289, 1990.

[Sco92]   B. D. Scott. "The mechanism of self sustainment in collisional drift wave turbulence." *Phys. Fluids B*, **4**:2468, 1992.

[Sco02]   B. D. Scott. "The nonlinear drift wave instability and its role in tokamak edge turbulence." *New J. Physics*, **4**:52.1–52.30, 2002.

[Sco03]   B. D. Scott. "Computation of electromagnetic turbulence and anomalous transport mechanisms in tokamak plasmas." *Plasma Phys. Control. Fusion*, **45**:A385–A398, 2003.

[Sco05]   B. D. Scott. "Drift wave versus interchange turbulence in tokamak geometry: Linear versus nonlinear mode structure." *Phys. Plasmas*, **12**:062314, 2005.

[SCR12]   D. A. Schaffner, T. A. Carter, G. D. Rossi, D. S. Guice, J. E. Maggs, S. Vincena, and B. Friedman. "Modification of Turbulent Transport with Continuous Variation of Flow Shear in the Large Plasma Device." *Phys. Rev. Lett.*, **109**:135002, 2012.

[Sta00]   P. C. Stangeby. *The plasma boundary of magnetic fusion devices.* Institute of Physics Publishing, 2000.

[TBG06]   P. W. Terry, D. A. Baver, and S. Gupta. "Role of stable eigenmodes in saturated local plasma turbulence." *Phys. Plasmas*, **13**:022307, 2006.

[TBH09]   P. W. Terry, D. A. Baver, and D. R. Hatch. "Reduction of inward momentum flux by damped eigenmodes." *Phys. Plasmas*, **16**:122305, 2009.

[TG06]   P. W. Terry and R. Gatto. "Nonlinear inward particle flux component in trapped electron mode turbulence." *Phys. Plasmas*, **13**:062309, 2006.

[TGB02]   P. W. Terry, R. Gatto, and D. A. Baver. "Nonlinear Damping of Plasma Zonal Flows Excited by Inverse Spectral Transfer." *Phys. Rev. Lett.*, **89**:205001, 2002.

[UPC11]   M. V. Umansky, P. Popovich, T. A. Carter, B. Friedman, and W. M. Nevins. "Numerical simulation and analysis of plasma turbulence the Large Plasma Device." *Phys. Plasmas*, **18**:055709, 2011.

[Wes04]   J. Wesson. *Tokamaks.* Clarendon Press, 2004.

[XRD93]   X. Q. Xu, M. N. Rosenbluth, and P. H. Diamond. "Electron-temperature-gradient-driven instability in tokamak boundary plasma." *Phys. Fluids B*, **5**:2206, 1993.

[ZBD96]   A. Zeiler, D. Biskamp, J. F. Drake, and P. N. Guzdar. "Three-dimensional fluid simulations of tokamak edge turbulence." *Phys. Plasmas*, **3**:2951, 1996.

[ZDB97]   A. Zeiler, J. F. Drake, and D. Biskamp. "Electron temperature fluctuations in drift-resistive ballooning turbulence." *Phys. Plasmas*, **4**:991, 1997.